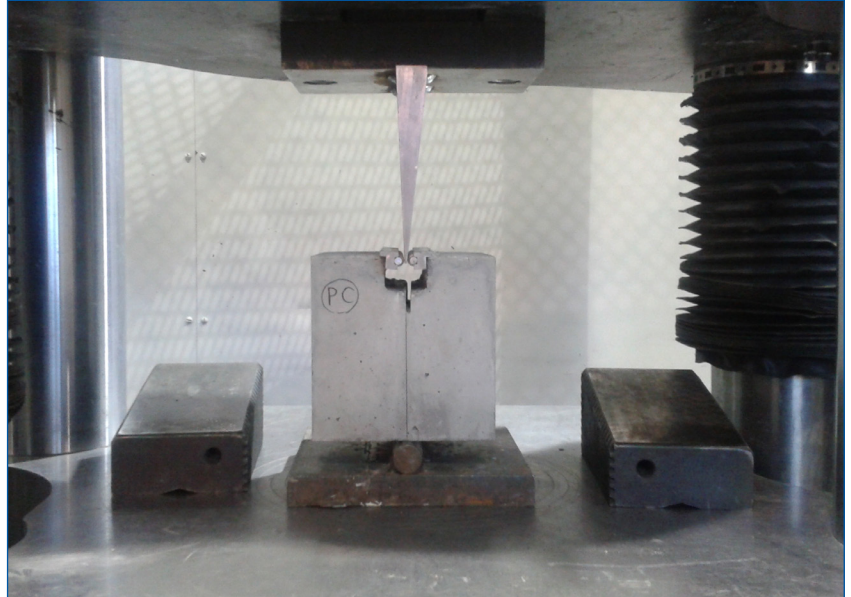


MOUNTAIN-PLAINS CONSORTIUM

MPC 17-319 | M. Kim and A. Bordelon

Cracking and Debonding
of a Thin Fiber Reinforced
Concrete Overlay



A University Transportation Center sponsored by the U.S. Department of Transportation serving the Mountain-Plains Region. Consortium members:

Colorado State University
North Dakota State University
South Dakota State University

University of Colorado Denver
University of Denver
University of Utah

Utah State University
University of Wyoming

**CRACKING AND DEBONDING OF THIN FIBER REINFORCED
CONCRETE OVERLAYS**

Min Ook Kim
Graduate Research Assistant
Department of Civil and Environmental Engineering

Amanda Christine Bordelon, Ph.D., P.E.
Assistant Professor
Department of Civil and Environmental Engineering

University of Utah

April 2017

Acknowledgements

The authors would like to thank the Mountain Plains Consortium Project 419; University of Utah Department of Civil Engineering; and Utah Department of Transportation for providing funding for this research. The authors thank the initial reviewers of this project idea for their useful feedback on topic, as well as thank the academic supervisory committee of Dr. Chris Pantelides, Dr. Pedro Romero, Dr. Luis Ibarra, and Dr. Eunhye Kim for their valuable comments and suggestions.

Disclaimer

The contents of this report reflect the views of the authors, who are reasonable for the facts and the accuracy of the information presented. This document is disseminated under the sponsorship of the Department of Transportation, University Transportation Centers Program, in the interest of information exchange. The U.S. Government assumes no liability for the contents or use thereof.

NDSU does not discriminate in its programs and activities on the basis of age, color, gender expression/identity, genetic information, marital status, national origin, participation in lawful off-campus activity, physical or mental disability, pregnancy, public assistance status, race, religion, sex, sexual orientation, spousal relationship to current employee, or veteran status, as applicable. Direct inquiries to Vice Provost for Title IX/ADA Coordinator, Old Main 201, NDSU Main Campus, 701-231-7708, [ndsu.eoaa.ndsu.edu](https://www.ndsu.edu/eoaa).

ABSTRACT

Previous field studies suggested that macro-fibers incorporated in thin overlay pavements will result in reduced crack opening widths, vertical deflections, and debonding rates compared to that of unreinforced overlays. A simple finite element (FE) model was developed and utilized in this study to investigate how fracture energy can affect the cracking and debonding of thin concrete overlays subjected to environmental loads. It was confirmed that crack opening width, vertical lift-off, and debonding rate all decrease as the fracture energy across a joint increases or as the interfacial tensile bond increases. The developed FE model also used to make a comparison between fiber-reinforcement and dowel-bar reinforcement across a joint. With larger amounts of reinforcement across the joint, either by higher fiber contents or by larger diameter dowels, the crack opening width, vertical lift-off and debonding rates were all reduced. Experimental tests were carried out to measure the tensile and shear bond strengths of an interface between an aged concrete and a newly cast fiber reinforced mortar overlay. It was found that the tensile interfacial energy increased with fiber-reinforcement; however, the interfacial fracture occurred through the overlay mixture and was proportional to the number of fibers which intersected the fracture path near this interface. It was confirmed that no statistical trend could be found between the tensile or shear bond properties and the addition of fibers. Overall, a reduction in debonding exhibited in the field was explained because the fiber-reinforcement reduced curling-induced lift-off, according to the finite element results.

TABLE OF CONTENTS

1. INTRODUCTION.....	1
2. LITERATURE REVIEW	3
2.1 FRC Properties.....	3
2.1.1 FRC Overlay Interfacial Bond	3
2.1.2 FRC Toughness and Fracture Energy	3
2.1.3 FRC Shrinkage.....	4
2.2 Pavement Design	4
2.2.1 Response due to Environmental Loading.....	4
2.2.2 Failures with Thin Overlays.....	5
3. FINITE ELEMENT ANALYSIS	6
3.1 Introduction.....	6
3.2 Field Project for Validation	6
3.3 Finite Element Model	10
3.4 Thin Overlay Input Effects	14
3.5 Dowel Bar versus FRC	17
3.5.1 FEM Configuration for Thicker Pavement	17
3.5.2 Comparison of Plain versus FRC in 150 mm overlay.....	20
3.6 FEM Findings	24
4. FIBER EFFECT ON INTERFACIAL BOND BETWEEN CONCRETE AND FIBER REINFORCED MORTAR.....	26
4.1 Introduction.....	26
4.2 Experimental Investigation	26
4.2.1 Materials and Test Variables.....	26
4.2.2 Bulk Material Property Tests	28
4.2.3 Composite Sample Fabrication	29
4.2.4 Wedge Split Tension Test	30
4.2.5 Bi-Surface Shear Test	30
4.3 Experimental Results and Discussion	31
4.3.1 Bulk Properties.....	31
4.3.2 Interface Tensile Splitting Results	33

4.3.3 Bi-Surface Shear Results.....	36
4.4 Experimental Bond Test Findings	39
5. CONCLUSIONS	40
REFERENCES.....	41

LIST OF TABLES

Table 3.1	Field Reported Flexural and Fracture Properties of FRC (Bordelon 2011)	9
Table 3.2	Applied Material and Fracture Properties for FEM.....	11
Table 3.3	Actual Averaged Field versus Darter-Barenberg or FEM Calculated Crack Widths.....	13
Table 3.4	Common Dowel Diameters (in.) Based on Pavement Thickness (Snyder 2011).....	17
Table 3.5	Applied Material and Fracture Properties for FEM.....	19
Table 3.6	Friction Coefficients Between Dowel and Concrete [from (Khazanovich et al. 2001)]	20
Table 3.7	Result of sensitivity analysis for 1.51 m (5 ft.) slab	21
Table 3.8	Result of sensitivity analysis for 4.60 m (15 ft.) slab	22
Table 4.1	Properties of Fibers	26
Table 4.2	Mix Design for Substrate Concrete and Fiber Reinforced Mortars.....	27
Table 4.3	Test Variables.....	28
Table 4.4	Fresh and Hardened Properties of Concrete and Fiber Reinforced Mortar	31
Table 4.5	Calculated P-Values Between Control Mortar versus FRM Mixture Strengths.....	32
Table 4.6	Results for Monolithically-Cast Wedge Splitting Mortar Samples.....	32
Table 4.7	P-values for Monolithically-Cast Splitting Tensile Force	32
Table 4.8	Results for Bonded Composite $\frac{1}{2}$ Concrete + $\frac{1}{2}$ Mortar Samples.....	35
Table 4.9	P-values for Bonded Samples.....	35
Table 4.10	Results for Bi-Surface Shear Test	38
Table 4.11	P-Values for Bi-Surface Shear Properties Between Control and FRM.....	38

LIST OF FIGURES

Figure 2.1	Influence of steel fibers on the debonding and cracking of repair layers.....	3
Figure 2.2	Schematic representation of fibers bridging across a crack under tension.....	4
Figure 2.3	Schematics of curling response in pavement slabs	5
Figure 3.1	Constructed full-scale thin FRC overlay, view of section 1.....	6
Figure 3.2	Summary of field project jointed slab sizes and pavement layer information	7
Figure 3.3	Measured free drying shrinkage and temperature (a) measured free drying shrinkage of concrete prisms collected from different truck batches on the day of construction; (b) measured field air temperature; (c) measured temperature differentials between top and bottom of FRC slab	8
Figure 3.4	Cracked-joint spacing and crack width at different measured ages of the field FRC overlays (a) measured cracked-joint spacing versus age; (b) measured average crack width versus age [reproduced data from (Bordelon 2011)]	10
Figure 3.5	Diagram shows the 2D modeling boundaries for the finite element analysis	11
Figure 3.6	Applied vertical deflections at the joint location for equivalent negative (nighttime) temperature gradient and shrinkage curling	12
Figure 3.7	Zoomed-in stress distribution showing cracking and debonding near the FRC joint for section 1 at 3-days shrinkage equivalent loading	13
Figure 3.8	Plot show how different fracture energy values in the FEM effect the crack width, debonding length, vertical deflection at the joint representing section 1 with 3-day equivalent loading	14
Figure 3.9	Effects of different FRC property on the crack opening width, debonding length, and vertical deflection at the joint representing section 1 in the model. (a) effect of tensile bond strength on w , L_{deb} , and δ_{lift} ; (b) effect of elastic modulus on w , L_{deb} , and δ_{lift} ; (c) effect of stiffness of elastic foundation on w , L_{deb} , and δ_{lift}	15
Figure 3.10	Effect of varying fracture energy on the crack width for (a) section 1 of 3.5 ft (1.12 m) joint spacing and (b) section 3 of 11 ft (3.35 m) joint spacing.....	16
Figure 3.11	Diagrams for (a) the 2D model boundaries; (b) finite element mesh.....	18
Figure 3.12	Modified coulomb model.....	20

Figure 3.13	Zoomed in stress distribution during cracking and debonding for (a) PCC without dowel; (b) FRC without dowel; (c) single dowel bar model ($\phi = 25$ mm dowel bar, .457 mm long, 0.38 high friction coefficient) in PCC.....	21
Figure 3.14	(a) Crack widths/slab size and (b) vertical deflections for different amounts of total reinforcement	23
Figure 3.15	Zoomed in stress distribution during cracking of dowelled FRC overlay with the lowest friction coefficient shows separation of concrete from dowel at joint location.....	24
Figure 4.1	Interfacial wedge splitting tension test configuration and LVDT mounting.....	29
Figure 4.2	Bi-surface shear test configuration.....	31
Figure 4.3	Wedge splitting force versus COD curves for one replicate of each monolithically-cast mortar specimens, (a) showing zoomed in; (b) showing full displacement range	33
Figure 4.4	Interfacial splitting tension force versus crack opening displacement curves for composite specimens: (a) $\frac{1}{2}$ concrete + $\frac{1}{2}$ slender and long polymeric FRM; (b) $\frac{1}{2}$ concrete + $\frac{1}{2}$ long polymeric FRM; (c) $\frac{1}{2}$ concrete + $\frac{1}{2}$ short steel FRM.....	34
Figure 4.5	Plot shows the relation between G_{bond} and number of fibers at interface.....	36
Figure 4.6	Averaged shear load-displacement curves for composite samples: (a) $\frac{2}{3}$ concrete+ $\frac{1}{3}$ slender and long polymeric FRM; (b) $\frac{2}{3}$ concrete + $\frac{1}{3}$ long polymeric FRM; (c) $\frac{2}{3}$ concrete + $\frac{1}{3}$ short steel FRM	37
Figure 4.7	Plot shows the relation between f_s and number of fibers at interface	38

NOMENCLATURE

s	=	average crack spacing
L_{slab}	=	saw-cut joint spacing
H	=	slab thickness
w	=	average crack width
L_{deb}	=	debonding length
δ_{lift}	=	vertical deflection
ΔT_{slab}	=	linear temperature gradient from bottom to top of slab (negative for daytime and positive for nighttime)
ΔT_{air}	=	maximum minus minimum air temperature a 1-month timespan
$\Delta \varepsilon_{sh}$	=	shrinkage strain gradient between top and bottom of the slab
$\varepsilon_{sh,free}$	=	free shrinkage strain of concrete or composite
$\varepsilon_{sh,restrained}$	=	restrained shrinkage strain
α_T	=	coefficient of thermal expansion of FRC
Y1	=	slender and long polymeric fiber
Y2	=	long polymeric fiber
T	=	short steel fiber
L_f/D_f	=	fiber aspect ratio = fiber length/fiber effective diameter
F_{SP}	=	splitting force
$G_{FRC, 2.5mm}$	=	cut-off total fracture energy
G_{bond}	=	fracture energy for interface tensile bond
f_s	=	shear bond strength

EXECUTIVE SUMMARY

Cracking and debonding are two important considerations for the pavement maintenance as they are linked to the service life of structures. Thin concrete overlay structures are considered to have reduced crack opening widths, slab deflections, and debonding rates when they contain fiber reinforcements. However, the effect of incorporated macro-fibers in thin concrete overlays were not systematically investigated yet. In this regards, this research experimentally investigated whether macro-fiber can influence on bond (tensile or shear) properties at the interface with the underlying substructure. A wedge split tension test and bi-surface shear test were selected as methods to evaluate interfacial bonds. A simple two-dimensional (2D) numerical analysis was carried out and compared with real fiber-reinforced concrete (FRC) overlays subjected to temperature loading. Specifically, the developed finite element (FE) model was calibrated against field data of thin FRC overlays exposed to environmental loading. The finite element analysis was used to understand other pavement responses such as reduced debonding and deflections, which have been reported for other field FRC overlays.

The numerical results using developed 2D FE model indicated that crack width, vertical lift-off, and debonding length all decreased when the fracture energy increased, or when the interfacial tensile bond increased, as expected. The developed FE model was additionally modified to investigate the effect of dowels and make a comparison with fiber-reinforcements. When compared to a completely unreinforced pavement, dowel reinforcement reduced crack widths by three times, while the fracture response from a typical 0.5% volume fraction of polymeric FRC reduced crack widths only by 1.3 times. While dowels are only used in thicker pavements, the use of FRC instead of dowels could be justified as a viable option for these thin (< 150 mm) overlays, since the reinforcement still significantly reduces crack widths, debonding lengths, and vertical deflections.

In addition to equations and FE modeling, experimental tests were carried out to further understand why debonding is often lower in FRC overlays. Tensile and shear bond strength between an aged concrete and a newly cast fiber-reinforced mortar were investigated. It was found that tensile interfacial energy was higher with the fiber-reinforcement mixtures as an overlay, particularly because the fracture path occurred through the new fiber-reinforcement layer and was bridged by these fibers. No statistical trend could be found between the peak strengths associated with either tensile or shear bond and the addition of fibers in the overlay mixture. The debonding reduction reported from the field overlay projects is expected to be due to the reduced lift-off of the FRC overlay when subjected to temperature and shrinkage loading.

1. INTRODUCTION

Fiber-reinforced concrete (FRC) has been widely utilized to improve the performance of plain concrete and used in new infrastructure, and in rehabilitation, repair, and retrofits (ACI Committee 544 1993; Banthia and Sheng 1996; Banthia et al. 1996; Gilbert et al. 2012; Grzybowski and Shah 1990; Jenq and Shah 1986; Kim and Bordelon 2015; Kim 2016; Kim and Bordelon 2016; Kim and Bordelon 2017; Li et al. 1993; Song et al. 2005; Zollo 1997). The principal role of the fibers is to control crack widths and growth rates of FRC by resisting tensile opening across the cracks (Mindess et al. 2002). A reduced crack width has been linked to this fiber-bridging effect of FRC (Banthia et al. 1996; de Oliveira e Sousa and Gettu 2006; Guo et al. 1999; Wang et al. 1990). Recently, use of FRC for ultra-thin (<4" or 100 mm thick) overlays on asphalt pavement has become increasingly popular in pavement rehabilitation (Banthia et al. 2004; Harrington 2008; Roesler et al. 2008). Fibers may be of particular benefit to thin overlays, because they minimize the crack widths, reduce surface spalling, and increase wear resistance (Rasmussen and Rozycki 2004). Pavements that are very thin (< 6" or 150 mm) do not have enough depth to have embedded dowels for reduction in vertical deflections or improved load transfer efficiencies at the joints. As such, fibers are expected to be beneficial as joint reinforcement for these thin overlays, since they also have been reported to reduce deflections and increase load transfer efficiencies (Cervantes and Roesler 2009).

Pavement cracking and debonding are mainly caused by stress differences between the overlay and substrate. These stresses can originate from relative humidity gradients, temperature gradients, and applied traffic loads (Denarié and Silfwerbrand 2004). Concrete slabs undergo volume changes due to changes in environmental conditions, such as humidity and temperature. Physically, slab curling occurs due to different drying shrinkage and temperature from the top to the bottom of the slab. The volume changes along with restraint and friction create internal stress that leads to cracking at the surface of the concrete overlay or cracking (later leading to debonding) at the interface between the layers (Lange and Shin 2001). According to several researchers, relative humidity-based shrinkage is considered the single most important factor determining service life of concrete overlay (Granju et al. 2004; Rahman et al. 2000; Weiss et al. 1998; Yuan et al. 2003). The effects of drying shrinkage and temperature gradients on pavement systems have been studied several times (Al-Qadi et al. 2005; Aure and Ioannides 2012; Ioannides 2005; Kohler and Roesler 2004; Lederle and Hiller 2012; Tompkins et al. 2012). These studies have developed empirical equations, or calibration factors for pavement design guide procedures to estimate volumetric changes and slab curling responses.

In concrete pavements, construction joints are placed at a certain spacing to reduce the net curling deformation and to localize potential cracking to a specific known location. If the joints are too close, the cost of saw-cutting for more joints will increase and the ride quality can decrease. If the joints are too sparse, slabs can curl significantly, mid-panel cracks are common, and again the ride quality can decrease. For thin overlay slabs constructed at 4 to 6" in thickness, the common practice guidelines recommend joints be placed at 12 to 18 times the pavement thickness (or 4 feet to 9 feet in this case) (Rasmussen and Rozycki 2004). One FRC overlay study by Carlswärd (Carlswärd 2006) considered that the crack opening width depends mainly on two factors; the extent of debonding and the effect of fibers bridging the crack. It was found that joints that cracked at early ages (within the first seven days) after placement of the concrete, were then always the widest cracks at later-ages (McCullough and Dossey 1999). This implies that understanding cracking and debonding against age-dependent properties of FRC is significant for maintenance of FRC overlay pavement structures.

The main objective of this research is to predict the crack widths of a thin fiber reinforced concrete overlay subjected to temperature gradients. A secondary objective is to study the dowel bar effect on reduced crack width compared to macro-fiber with using numerical analysis. A third objective is to investigate the effect on fiber on tensile and shear interfacial bonds between an aged substrate concrete and the new fiber reinforced mortar overlay.

2. LITERATURE REVIEW

2.1 FRC Properties

2.1.1 FRC Overlay Interfacial Bond

Since stresses from differential expansion and contraction are the highest at boundaries, such as cracks, joints or edges, these stresses can lead to debonding (Delatte et al. 2000). If the vertical and axial stresses at the interface exceed the bond strength between the overlay and substrate, the overlay will begin to debond. Debonding of the overlay from the underlying substrate can be a separate phenomenon or concurrent with the effects of shrinkage curling and loading strains in a pavement slab. Field experimental studies (Chanvillard et al. 1989; Delatte et al. 2000) have suggested a stronger bond occurs with steel macro-fiber reinforced concrete (SFRC) overlays as compared to unreinforced or polymeric macro-fiber reinforced concrete (PFRC). The effect of steel fibers on debonding were further investigated in a laboratory and it was found that steel fiber does not increase bond strength itself, but delays crack opening rate after crack initiation (Granju 1996). Figure 2.1 shows some results from the article (Granju 1996). A SFRC mixture containing 1.0% V_f was found to have initial debonding when the first crack developed through the overlay, yet exhibited delay in propagation of the debonded area. A different steel fiber type at 0.4% V_f exhibited no debonding itself in this experiment by Granju.

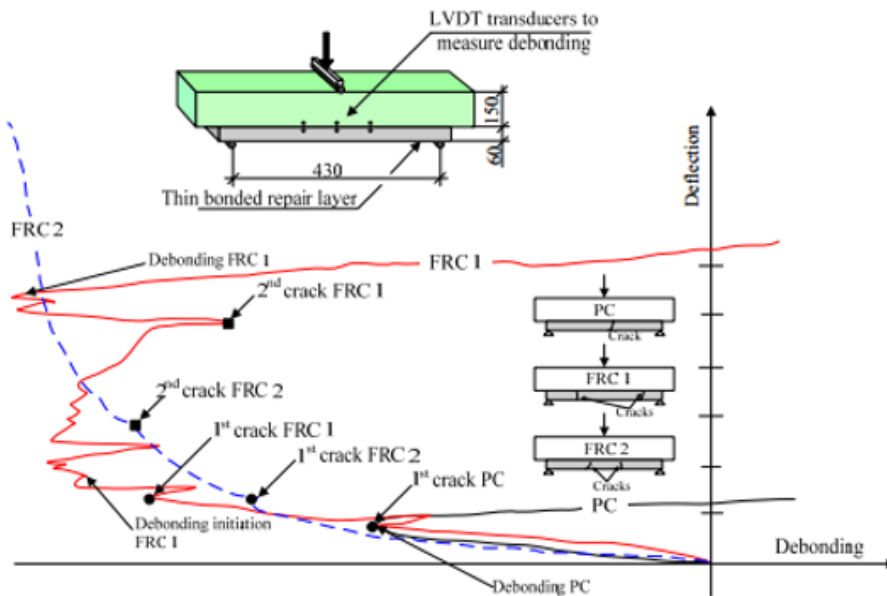


Figure 2.1 Influence of steel fibers on the debonding and cracking of repair layers (Granju 1996).

2.1.2 FRC Toughness and Fracture Energy

FRC is primarily noted for improving toughness and fracture energy (Banthia and Sheng 1996; Jenq and Shah 1986; Kim and Bordelon 2015; Li et al. 1993; Song et al. 2005; Wang et al. 1990). Figure 2.2 shows a schematic representation of fibers bridging across a crack under tension. There is a traction-free zone, where the crack is wide enough for all fibers to have pulled out; a fiber-bridging zone in which stresses are transferred by frictional slip of the fibers; and a micro-cracked matrix process zone with enough aggregate interlock to transfer some stress within the matrix itself (Mindess et al. 2002). At the fiber-bridging zone, the matrix can not carry load across the crack surface, but the fibers carry all post-cracking loads taken by the composite. In this bridging zone, the fibers will tend to transfer tensile stress to the

matrix through shear frictional bond stresses. Residual strength ratio is the ratio between FRC flexural strength and residual strength. Residual strength ratio is commonly used for the design of fiber reinforced concrete overlay. Fracture energy is the required energy for crack initiation and propagation. Total fracture energy is commonly used to define the fracture behavior of FRC in the finite element modeling. Of the two properties, the residual strength ratio has been more commonly adopted for thin FRC overlay designs to-date (Bordelon and Roesler 2012; Harrington and et al. 2014), while fracture energy may be more fundamental and used by other researchers in finite element analysis, but has not been adopted as a standard tested property (Bordelon 2011; Gaedicke et al. 2012; Roesler and Khazanovich 1997).

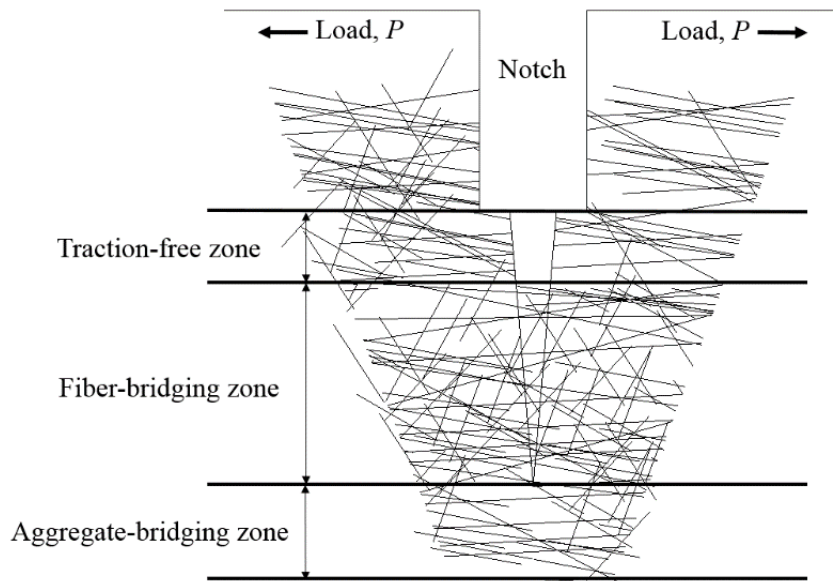


Figure 2.2 Schematic representation of fibers bridging across a crack under tension.

2.1.3 FRC Shrinkage

Shrinkage is reported as a leading contributor to slab curling joint opening, and widening of cracks found in pavements. Although this research only focuses on use of macro-fibers, the use of micro-fibers at low volume fraction ($V_f < 1\%$) are commonly thought to reduce shrinkage cracking (Mehta and Monteiro 2006). This phenomenon is controversial as some experimental studies have demonstrated a reduction in shrinkage and others show negligible effects on shrinkage (Balaguru and Ramakrishnan 1988; Mangat and Azari 1988; Sanjuan 1999; Swamy and Stavrides 1979). For the finite element analysis study, the shrinkage values used were from the field-constructed samples made at the same time of the same material as the actual field-constructed and environmentally-loaded overlay.

2.2 Pavement Design

2.2.1 Response due to Environmental Loading

Figure 2.3 shows schematic figures of shrinkage curling and temperature curling in any typical pavement design. The pavement slabs can be exposed to significant temperature and moisture gradients, depending on temperature and moisture exposure conditions. Besides the general environmental curling response, both temperature and moisture gradient occurring in the slab at the time of setting can create a permanent curling response, called “built-in-curling.” Temperature and moisture gradients can cause slabs to curl to either greater magnitudes or may actually act counter to the built-in-curling and produce a slab that appears un-curved. The weight of the slab on high curling deformation can sometimes be high enough to

create a flexural stress that exceeds the strength of a slab and causes a mid-panel crack to form. A typical joint opening for a 4.6 m-spaced (15 foot) jointed pavement subjected to thermal and shrinkage loading alone was reported to be between 0.76 and 1.9 mm (Roesler and Wang 2008). In this study, similar thermal loading is applied, but the overlay design investigated considers shorter slab sizes. According to the Darter and Barenberg model for joint opening in un-reinforced pavements (Darter and Barenberg 1977), a shorter slab size of 1.1 m (3.6 feet) could be expected to see a range of joint opening from 0.18 to 0.46 mm from this thermal loading alone.

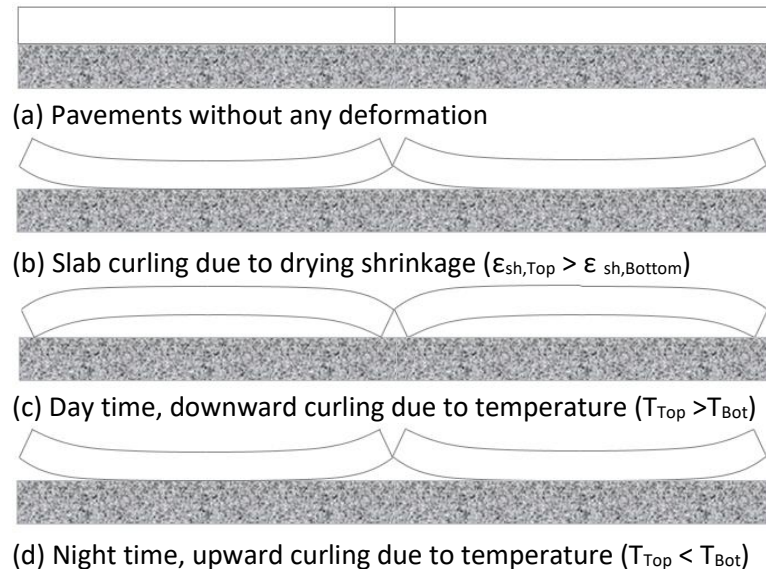


Figure 2.3 Schematics of curling response in pavement slabs.

2.2.2 Failures with Thin Overlays

Thin bonded overlay-substrate composites are intended to move monolithically, and the bond at the interface ensures continuity of deformations between the overlay and base. Common failure mechanism for thin overlays are corner breaks (Akers and Warren 2005; King and Roesler 2014; Vandenbossche and Rettner 1999), possibly due to debonding and vertical lift-off near the closely spaced joints and corners. Some researchers (Emmons et al. 2000; Vaysburd and Emmons 2000) have stated that whenever debonding is found, corner cracking typically will occur. Many possible causes of debonding initiation occur, even for properly placed overlays, and include: extreme ambient temperatures or moisture conditions during construction, improper moist curing, subsequent freezing and thawing, water penetration through fine cracks, and dynamic vehicle impact due to surface roughness or faulting. From a mechanical respect, it is widely accepted that two classes of debonding causes exist: effects of the external mechanical loading and effects of the different volumetric changes between the overlay and its substrate. It also is known that debonding initiates preferentially near overlay boundaries, cracks, and joints.

3. FINITE ELEMENT ANALYSIS

3.1 Introduction

The predicted crack widths are validated against field project data of a 50 mm (2 in.) constant slab thickness and constant FRC mixture (Bordelon 2011). The project had different joint spacing from 3.5 to 11 feet (1.12 to 3.35 m) subjected to only environmental loading for six years, rather than traffic loading. A finite element model was generated to determine how variation in the FRC fracture energy across the joint, magnitude of shrinkage, and the joint spacing may affect the overlay's cracked joint width, vertical lift-off, and debonding length.

3.2 Field Project for Validation

Measurements from a previously constructed full-scale 50 mm thin FRC pavement (Bordelon 2011; Bordelon and Roesler 2011), as shown in Figure 3.1, were utilized for this study to validate the new crack width finite element analysis. The field overlay pavement was constructed in Rantoul, Ill., in the summer of 2009, and this climate exhibits some significant temperature and humidity fluctuations throughout the year. This full-scale experiment has only been subjected to environmental loading at the time of this research. No traffic loads have been applied to this pavement since casting.



Figure 3.1 Constructed full-scale thin FRC overlay, view of section 1.

The pavement mixture contained a hybrid of fibers: a 40 mm-long polypropylene-polyethylene-blended slender and long structural macro-fiber ($L_f/D_f = 90$), and a 6 mm-long polypropylene micro-fiber ($L_f/D_f = 300$), at 0.48 and 0.06 percent V_f , respectively. The mixture contained a higher cementitious content of 417 kg/m^3 than normal paving mixtures to coat the fibers more thoroughly. The FRC overlay was roughly 50 mm thick, constructed on a milled aged hot mixed asphalt (HMA) pavement and cut at three different slab sizes, as illustrated in Figure 3.2.

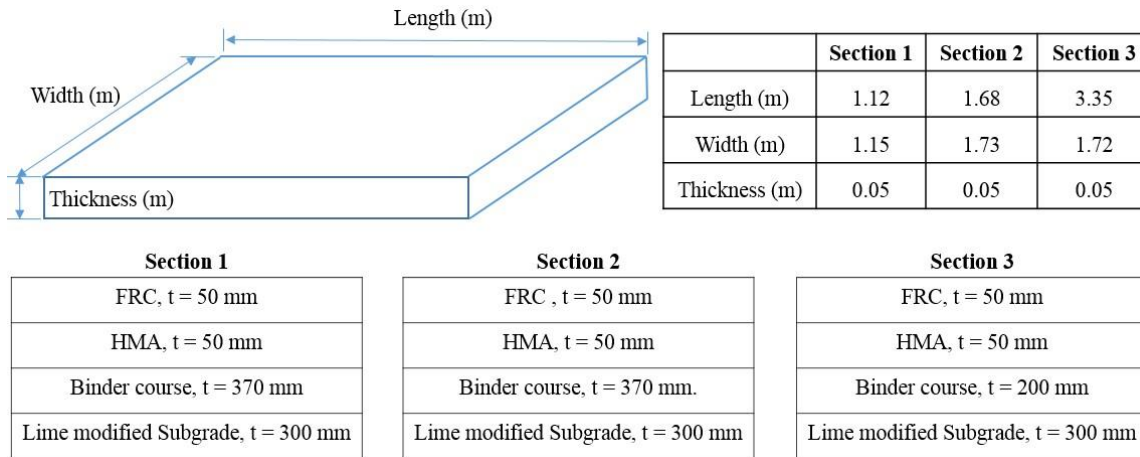


Figure 3.2 Summary of field project jointed slab sizes and pavement layer information (Bordelon 2011).

Figure 3.3(a) shows the recorded free drying shrinkage values for samples cast in the field, but measured in a controlled 50% RH and 22°C environment. Figure 3.3(b) and Figure 3.3(c) show the ambient air temperature and measured temperatures from thermocouples installed at the top and bottom of the FRC slab. The temperature difference from the top to the bottom of the FRC slab at any given time of day was approximately $\Delta T = 2^\circ\text{C}$, and will be an input for determining thermal loading in the finite element model.

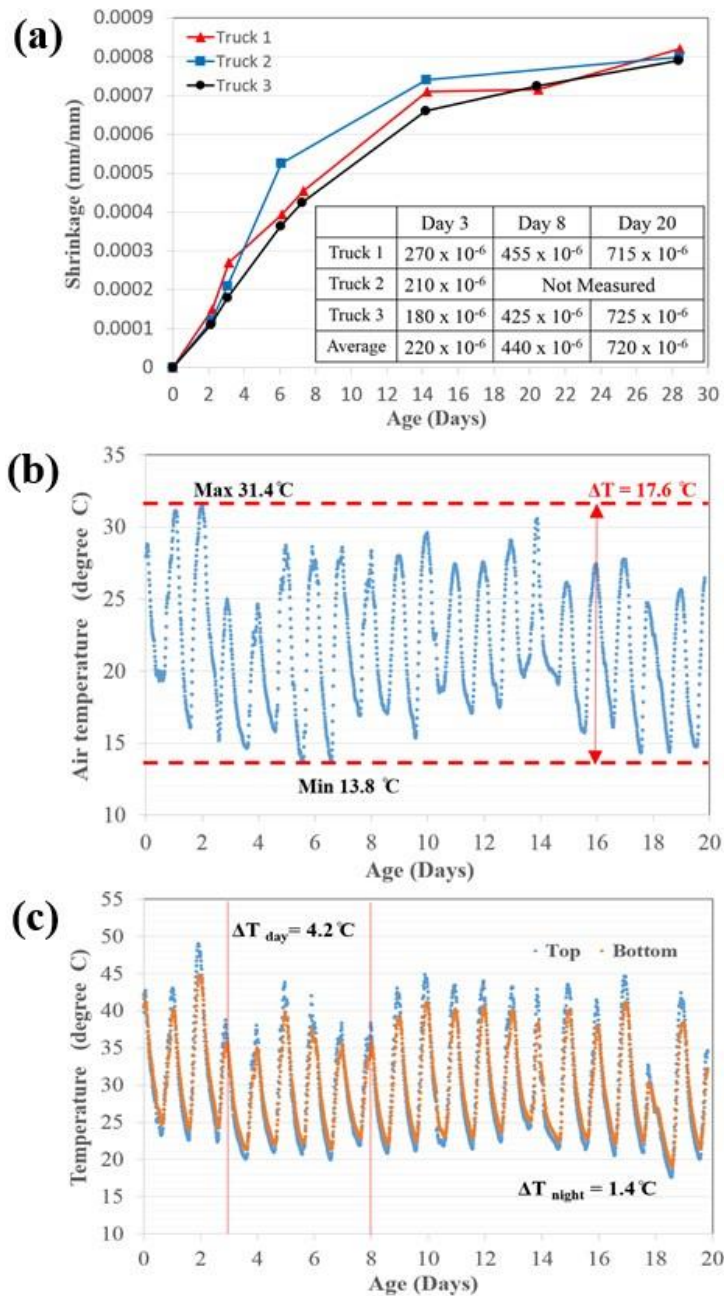


Figure 3.3 Measured free-drying shrinkage and temperature (a) measured free-drying shrinkage of concrete prisms collected from different truck batches on the day of construction; (b) measured field air temperature; (c) measured temperature differentials between top and bottom of FRC slab.

Table 3.1 shows the reported lab-cast flexural and fracture specimen properties of the FRC mixture. The flexural strength f_1 , residual strength f_{L150} , and residual strength ratio R_{150} were determined according to ASTM C1609. Two different sizes of beam (75mm or 150 mm deep) were tested at 7 days and 28 days for flexural properties of FRC. The split-tensile strength of the FRC $f_{t,FRC}$ was measured according to ASTM C496. The fracture properties G_f , G_{FRC} , and $CTOD_c$ of FRC were determined from a three-point bending test results of a single-edge notched beam (SEN[B]) according to the Two Parameter model (Jenq and Shah 1986) and Hillerborg method (Hillerborg 1985).

Table 3.1 Field Reported Flexural and Fracture Properties of FRC (Bordelon 2011)

Age (days)	Flexural						Tensile	Fracture		
	7.5 x 7.5 cm beam			15 x 15 cm beam			$\phi 10 \times 20$ cm	15 x 8 x 70 cm SEN[B]		
	f_1	f_{L150}	R_{75}	f_1	f_{L150}	R_{150}	$f_{t,FRC}$	G_f	G_{FRC}	$CTOD_c$
	(MPa)	(MPa)	(%)	(MPa)	(MPa)	(%)	(MPa)	(N/m)	(N/m)	(mm)
7	4.49	2.19	48.8	3.78	1.80	47.6	3.49	63.2	3691	0.026
28	4.77	2.12	44.4	5.02	1.41	28.0	4.25	52.8	3175	0.019

Debonding was investigated in the field project at roughly three months after construction using a chain drag and in-situ torsional test at specific cored locations. Based on these investigations, it was estimated that the potential for debonding was high for large portions of section 1, which counterintuitively had the smallest joint spacing. A torsional test on a limited number of samples (four cores) was found highly variable, yet the average bond strength was estimated to be 400 N-m between FRC and HMA after 75 days. The cracked joint spacing and crack widths were visually measured at 3, 8, and 20 days after construction.

A crack comparator card was used to visually interpret the crack widths. Figure 3.4 shows the relationship between measured average cracked-joint spacing versus age and measured average crack width versus age, respectively. An important finding here was that only the joints cracked; there were no mid-panel cracks in the FRC overlay slabs. The larger slabs, representing the greatest average crack spacing, also had the largest crack widths, as expected.

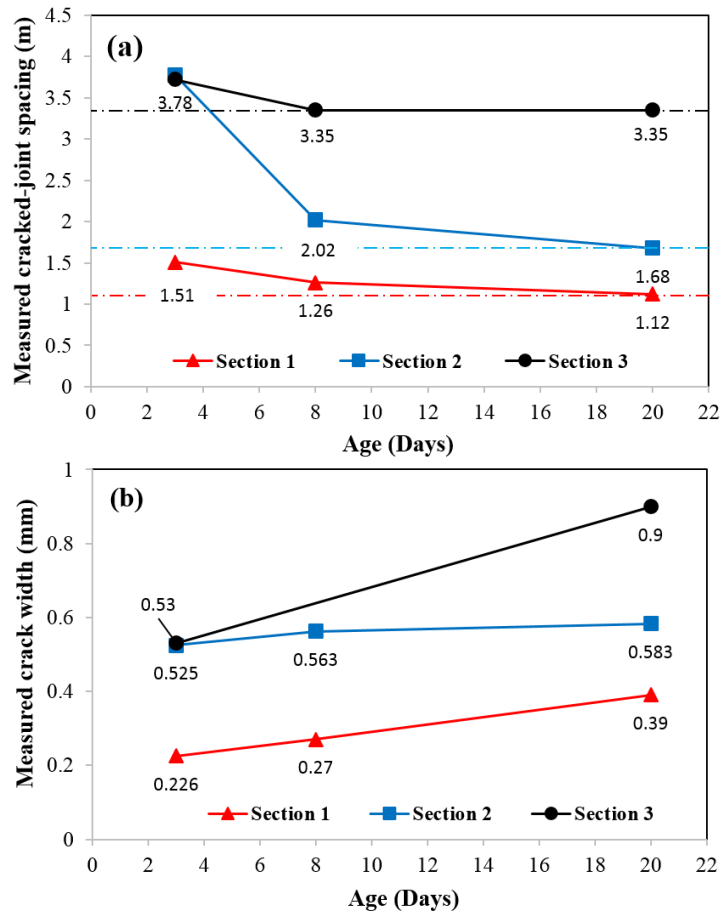


Figure 3.4 Cracked-joint spacing and crack width at different measured ages of the field FRC overlays (a) measured cracked-joint spacing versus age; (b) measured average crack width versus age [reproduced data from (Bordelon 2011)].

Not all joints cracked after the first temperature cycle at the earliest ages, despite an exhibited 10°C of air temperature differential in the first day. Still cracks that formed day one remained the largest at later ages, as seen also by researchers, who also investigated jointed pavements (McCullough and Dossey 1999).

3.3 Finite Element Model

A finite element model was created as a two-dimensional analysis focusing on crack opening widths and debonding of the FRC overlay. Three different model geometries were created of each field slab size (1.12, 1.68, and 3.35 m) and their corresponding underlying structural pavement thickness according to Figure 3.2. Three shrinkage loading levels also were studied to estimate a relative age-effect on pavement responses. Other material properties were studied after the basic geometry and loading configurations were analyzed.

The model geometry consists of two side-by-side FRC half-slabs supported by HMA and subgrade as illustrated in Figure 3.5. The HMA and underlying binder base-course properties (as shown in Table 3.2) were assumed to be constant at all ages to simplify the model. The subgrade was idealized as an elastic foundation that can only support compression.

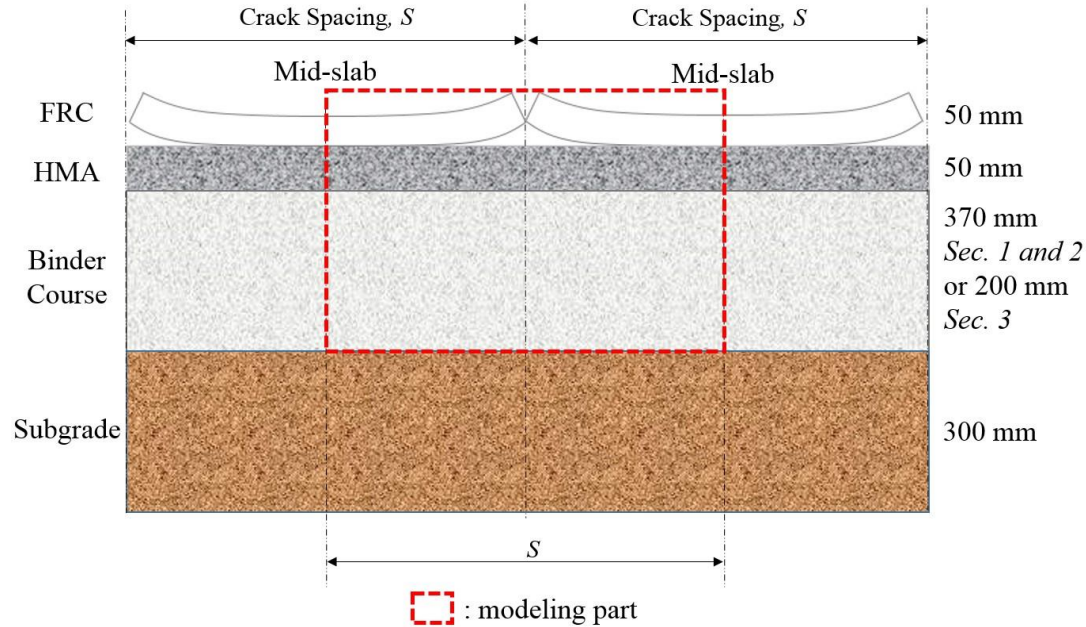


Figure 3.5 Diagram shows the 2D modeling boundaries for the finite element analysis.

Table 3.2 Applied Material and Fracture Properties for FEM

Layer	Material Property	Value
FRC	Density (kg/m ³)	2313
	Elastic Modulus (GPa)	31.7
	Poisson's ratio	0.15
	Coefficient of thermal expansion (/°C)	10 x 10 ⁻⁶
HMA	Density (kg/m ³)	2300
	Elastic Modulus (GPa)	2.75
	Poisson's ratio	0.30
Binder (sub-base)	Density (kg/m ³)	1900
	Elastic Modulus (GPa)	0.3
	Poisson's ratio	0.35
Cohesive Interface	Fracture Property	Value
Joint location at FRC layer	Penalty stiffness (Pa/m)	1 x 10 ¹²
	Fracture energy (N/m)	Varies (80 to 3500)
	Tensile strength (MPa)	2.0
FRC-HMA interface	Penalty stiffness (Pa/m)	1 x 10 ¹²
	Fracture energy (N/m)	70
	Tensile bond strength (MPa)	0.5

In this study, an elastic foundation stiffness value of 150 kPa/mm was applied as the default to create a worst-case curling scenario (Gaedicke and Roesler 2009). A saw-cut joint which has 3 mm of width and 12 mm of depth was created in the model geometry to match the field construction.

For each model of geometry, a calculated equivalent thermal load was applied at specific ages (3, 8, and 20 days) rather than a time-dependent model. The magnitude of the thermal load was applied as an equivalent vertical deflection δ_T , shown as Eq. (3.1) based on the back-calculated shrinkage gradient and temperature gradient expected at that age. Both shrinkage and temperature were simplified to be linear gradients for this study. The top of the FRC layer was assumed to be subjected to the same free drying

shrinkage as shown in Figure 3.3(a). The direction and location of the applied displacement is shown schematically in Figure 3.6. No other external constraints were applied to the FRC slabs.

$$\delta_T = \frac{(\Delta\varepsilon_{sh} + \alpha_T \Delta T_{slab}) L_{slab}^2}{2H} \quad (3.1)$$

where $\Delta\varepsilon_{sh}$: shrinkage strain gradient between the top and bottom of the FRC slab (mm/mm); α_T : coefficient of thermal expansion of FRC (mm/mm-°C); ΔT_{slab} : linear temperature difference from the bottom to the top of the concrete slab (°C), assumed to be 2 °C for the field 50 mm overlay as stated previously or this was expanded to be 6 °C when studying an equivalent 150 mm overlay; L_{slab} : saw-cut joint spacing (mm); H : slab thickness (mm); $\varepsilon_{sh,free}$: measured free shrinkage strain based on experimental data (mm/mm) for the top surface of the slab; $\varepsilon_{sh,restrained}$: estimated restrained shrinkage strain of 25×10^{-6} mm/mm for the bottom of a concrete slab cast against aged concrete (Gilbert et al. 2012).

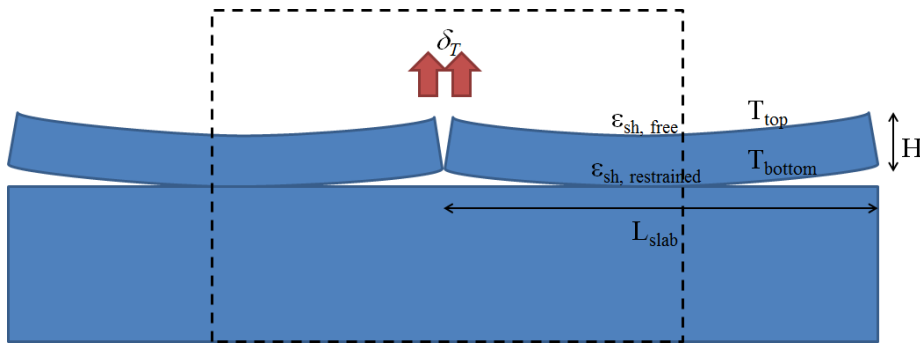


Figure 3.6 Applied vertical deflections at the joint location for equivalent negative (nighttime) temperature gradient and shrinkage curling.

The contact areas across both the vertical joint location in the FRC and the FRC-HMA interface underneath the overlay were defined using surface-based cohesive behaviors (ABAQUS 2001). Although researchers have indicated a trilinear traction-separation is most suitable to describe the full post-cracking response of FRC (Park et al. 2008; Roesler et al. 2007), a linear traction-separation law was applied for simplicity on both cohesive interfaces. This assumed an initial elastic behavior as defined by a penalty stiffness. In this case, 1×10^{12} Pa/m was applied (Gaedicke and Roesler 2009). After a maximum tensile strength is reached in the cohesive interface, a damage evolution is initiated. Debonding at the FRC-HMA interface is defined for nodes where this damage initiation has begun. Traction carried across interfaces is defined based on the fracture energy and tensile strength of material. Table 3.2 shows the defined material and fracture properties in the model.

Figure 3.7 shows a zoomed-in view of the stress distribution of the developed model, which can assist in visualizing the near-joint effects of a single daytime thermal gradient and shrinkage load. The model predicts that at this thermal magnitude of 0.4 °C/mm, a crack and some debonding will occur, as in many of the slabs in the field project. The developed model is not a time-dependent model. Thus, a step in the Figure 3.7 indicates a unit of computation time. In this case, step 8 indicates the achieved full thermal gradient magnitude applied in the analysis.

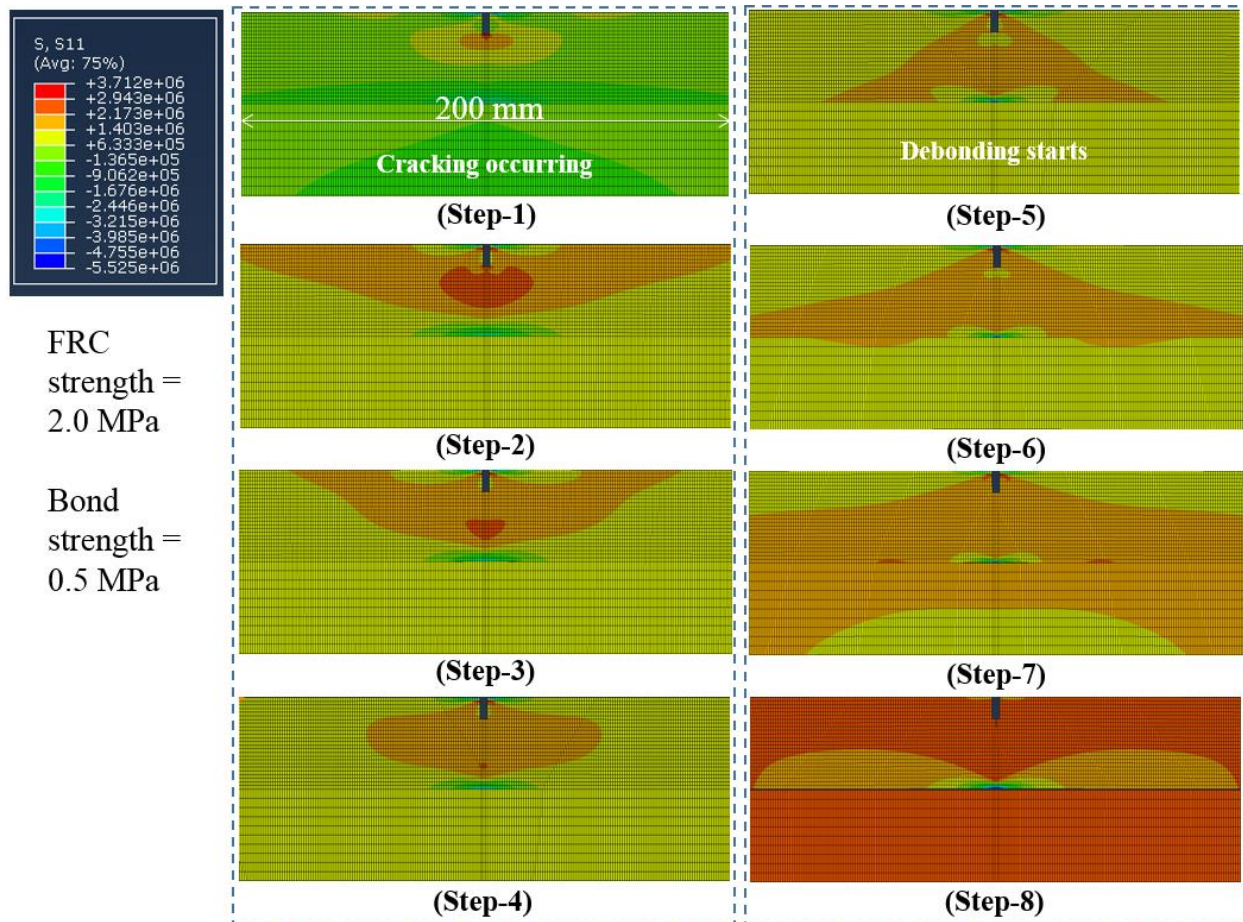


Figure 3.7 Zoomed-in stress distribution showing cracking and debonding near the FRC joint for section 1 at three days shrinkage equivalent loading.

The calculated crack widths from the numerical analysis were compared to crack widths from the field observation, as shown in Table 3.3. The calculated crack widths for section 1 and section 3 were within 18% or less than 0.04 mm difference of the actual experimental measurements. It was anticipated that the actual crack width for section 2 by the eight-day age was uniquely high either from human reading error or from material variability. Even with this one highly variable reading for section 2, the FEM was within 0.17 mm difference of the actual averaged field crack widths. The Table 3.3 also shows predicted crack widths according to the Darter-Barenberg model (Darter and Barenberg 1977) which is the pavement design standard practice calculation for joint opening based on thermal and shrinkage loading alone. In most cases, this Darter-Barenberg model, which assumes the concrete is un-reinforced, overestimates the crack widths of the FRC overlay.

Table 3.3 Actual Averaged Field versus Darter-Barenberg or FEM Calculated Crack Widths

Age (days)	Section 1 (1.12 m)			Section 2 (1.68 m)			Section 3 (3.35 m)		
	Crack width (mm)								
	Actual	Darter-Barenberg	FEM	Actual	Darter-Barenberg	FEM	Actual	Darter-Barenberg	FEM
3	0.226	0.270 [+20%]	0.186 [-18%]	0.525	0.405 [-23%]	0.355 [-32%]	0.530	0.808 [+52%]	0.491 [-7%]
8	0.270	0.430 [+59%]	0.297 [+10%]	0.563	0.645 [+15%]	0.437 [-22%]	NA	1.287	0.645
20	0.390	0.634 [+63%]	0.362 [-7%]	0.583	0.951 [+63%]	0.608 [+0.4%]	0.900	1.897 [+111%]	0.889 [-1%]

Note: values in brackets indicate either +% over-predicted crack or -% under-predicted crack widths

3.4 Thin Overlay Input Effects

Effects of the input fracture energy across a cracked joint, the tensile bond strength at the interface, elastic modulus of the FRC, and stiffness of elastic foundation were investigated by using the developed model. For each of these varied parameters, the crack width (w), debonding length (L_{deb}), and vertical deflection (δ_{lft}) were recorded from the FEM. Section 1 at three-day age was selected for this sensitivity analysis. Deflections were not monitored in field observation and debonding was only measured after 20 days (while this study also investigates 3 and 8 days responses).

Fracture energy at the joint location was varied from 80 N/m to 3500 N/m to account for the possible expected range for plain un-reinforced concrete to the recorded total fracture energy of a 0.5% volume fraction PFRC at seven days (see Table 3.1), respectively. A unique finding made was that for section 1 (as shown in Figure 3.8), any input total fracture energy above about 200 N/m no longer further reduced the crack width, debonding length, or vertical lift off.

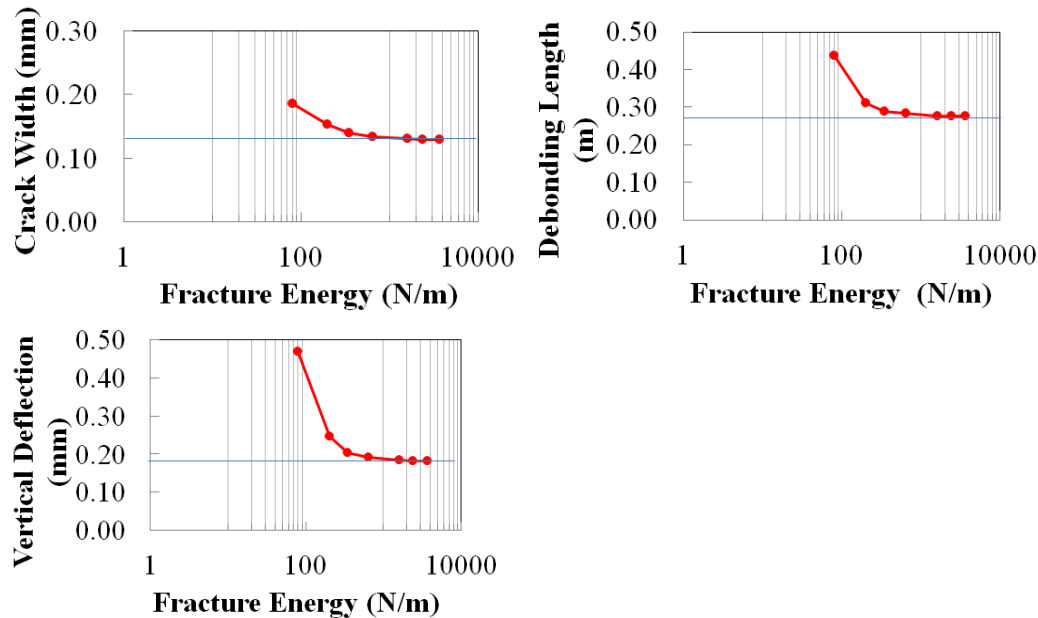


Figure 3.8 Plot shows how different fracture energy values in the FEM affect the crack width, debonding length, vertical deflection at the joint representing section 1 with three-day equivalent loading.

The tensile bonds between 0.5 and 2.5 MPa were selected according to the reference (Sprinkel and Ozyildirim 2000). 0.5 MPa represents the poor bond while 2.5 MPa of bond represents excellent. As illustrated in Figure 3.8 and Figure 3.7, w , L_{deb} , and δ_{lift} all decreased as either the fracture energy or interface tensile bond strength were increased.

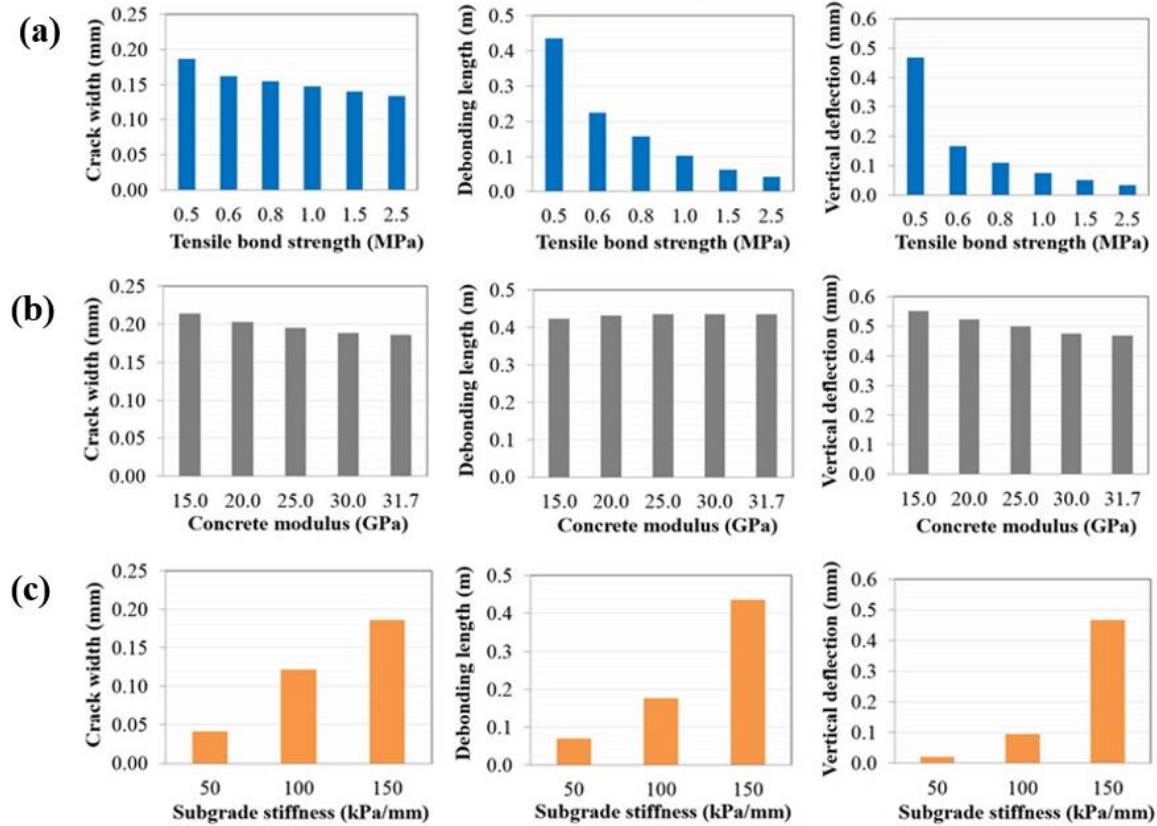


Figure 3.9 Effects of different FRC property on the crack opening width, debonding length, and vertical deflection at the joint representing section 1 in the model. (a) effect of tensile bond strength on w , L_{deb} , and δ_{lift} ; (b) effect of elastic modulus on w , L_{deb} , and δ_{lift} ; (c) effect of stiffness of elastic foundation on w , L_{deb} , and δ_{lift} .

It also was expected that a high elastic modulus would show greater w and L_{deb} (Lange and Shin 2001). As seen in Figure 3.9, the w and δ_{lift} actually unexpectedly decreased by 13% and 15%, respectively, as the concrete elastic modulus was increased from 15 GPa to 31.7 GPa. Meanwhile, L_{deb} was found in this study to not be affected by the range of elastic modulus studied.

Furthermore, it was found that the w , L_{deb} , and δ_{lift} all increased by 4, 6, and 22 times, respectively, with an increased stiffness of the elastic foundation from 50 kPa/mm to 150 kPa/mm. This trend is reasonable because it is expected that the softer soil with lower stiffness would have a lower deflection under the same pressure. Overall, sensitivity analysis indicated that the L_{deb} is not as affected by fracture energy and the elastic modulus of the FRC; or in-other-words, L_{deb} is influenced primarily by the subgrade stiffness and interfacial tensile bond strength between the FRC and underlying HMA.

Since crack width was still dominantly affected by the FRC fracture energy, but only up to a certain linear traction-separated fracture value of 200 N/m in section 1, a few additional sensitivity trials were performed to investigate whether a similar fracture energy limitation occurred with different slab geometries and loading levels. In this second sensitivity study, the extreme fracture energies of plain

concrete and FRC were performed on section 3 at each analyzed age (3, 8, and 20 days) of equivalent loading. These are shown graphically in Figure 3.10 for the crack width prediction. Unlike section 1 of the 3.5-foot shorter slab sizes, crack widths of the field section 3 with the 11-foot longer slabs were more closely matched when the full total 3500 N/m total fracture energy of the FRC was used in the FEM analysis. With a larger slab size, crack widths were reduced by approximately 11% when FRC fracture energy was 3,500 N/m, as compared to a plain concrete fracture energy of 80 N/m between 3 and 20 days.

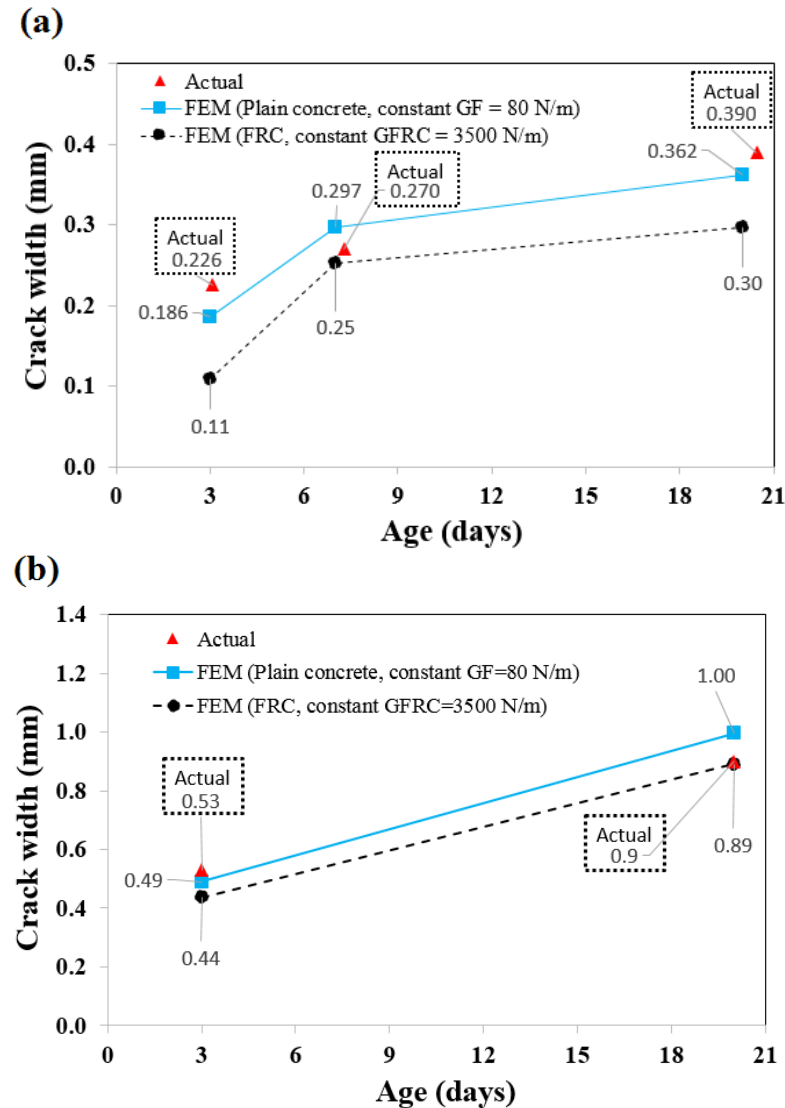


Figure 3.10 Effect of varying fracture energy on the crack width for (a) section 1 of 3.5-foot (1.12 m) joint spacing and (b) section 3 of 11-foot (3.35 m) joint spacing.

An important note to recall is that the smallest sized slabs (Section 1) in the field experimental data exhibited significant debonding during early ages while debonding was not systematically investigated. Further research might be necessary to investigate the correlation between fiber addition and debonding rate. The correlation between debonding and crack width in the presence of fiber reinforcement is thus not well understood. The magnitudes of debonding and vertical deflection in these FEM simulations were found to have negligible change with higher fracture energy values.

3.5 Dowel Bar versus FRC

Many pavements use dowel bar reinforcement at joints to reduce vertical deflections when pavement is loaded under traffic. The dowels help resist crack opening widths and debonding lengths besides this reduction in vertical deflection. For this study, a simple comparison between dowels and fiber-reinforcement was studied to determine which is more effective at reducing deflections, crack widths, and debonding.

In practice, dowels are not applicable in such thin 50 mm (2”) pavement sections. Thus, the thickness of overlay layer for this stage of the FEM analysis was increased to 150 mm (6”), which is more common when dowels are used. Joint spacings of 3.5 ft and 15 ft were compared in this study to either match up more closely with the previous analysis or to represent more realistic slab sizes of a 6” jointed plain concrete pavement. The material properties, load, contact, and boundary conditions used in the model were kept the same as in the previous model except for the increased overlay thickness and optional placement of a single dowel bar across the joint. As same with previous developed model, two cohesive zones were defined at interface between two FRC slabs side by side and also between FRC (top) and HMA (bottom) layer.

Crack opening width (w), debonding length (L_{deb}), and vertical deflection (δ_{lft}) were monitored and compared between dowelled versus un-dowelled and among plain versus FRC as the overlay material in the dowelled case. This study considered the effects of two commonly-found dowel diameters, three reported concrete-dowel friction coefficients, and three dowel lengths.

3.5.1 FEM Configuration for Thicker Pavement

Table 3.4 shows the summary of state practices concerning dowel bar diameter as a function of pavement thickness (Snyder 2011). It can be seen that dowels can be applicable at 150 mm (6”) slab thickness, and that most states use 25 mm (1”) dowel bar diameter for 150 mm (6”) thickness pavement.

Table 3.4 Common Dowel Diameters (in.) Based on Pavement Thickness (Snyder 2011)

Slab Thickness (in.)	6.0	6.5	7.0	7.5	8.0	8.5	9.0	9.5	10.0	10.5	11	11.5	12.0	12.5
California	1.250	1.250	1.250	1.250	1.250	1.500	1.500	1.500	1.500	1.500	1.500	1.500	1.500	1.500
Iowa	0.750	0.750	0.750	0.750	1.250	1.250	1.250	1.250	1.500	1.500	1.500	1.500	1.500	1.500
Illinois	1.000	1.000	1.250	1.250	1.500	1.500	1.500	1.500	1.500	1.500	1.500	1.500	1.500	1.500
Indiana	1.000	1.000	1.000	1.000	1.000	1.000	1.250	1.250	1.250	1.250	1.250	1.250	1.250	1.500
Michigan	1.000	1.000	1.000	1.000	1.250	1.250	1.250	1.250	1.250	1.250	1.250	1.500	1.500	1.500
Minnesota	1.000	1.000	1.250	1.250	1.250	1.250	1.250	1.250	1.250	1.500	1.500	1.500	1.500	1.500
Missouri	N/A	N/A	1.250	1.250	1.250	1.250	1.250	1.250	1.250	1.500	1.500	1.500	1.500	1.500
North Dakota	1.250	1.250	1.250	1.250	1.250	1.250	1.250	1.250	1.250	1.500	1.500	1.500	1.500	1.500
Ohio	1.000	1.000	1.000	1.000	1.000	1.250	1.250	1.250	1.250	1.500	1.500	1.500	1.500	1.500
Texas	N/A	N/A	N/A	N/A	1.000		1.125		1.250		1.375		1.500	
Wisconsin	N/A	N/A	1.000	1.000	1.250	1.250	1.250	1.250	1.500	1.500	1.500	1.500	1.500	1.500

Figure 3.11 shows dimensions of the model, modeling boundary, and finite element mesh. Two adjacent half-slabs 0.755 m or 2.3 m long were modeled, connected with a cohesive zone at the joint and an optional dowel bar placed at mid-height (75 mm) of the slab. Common practice for 150 mm (6”) thick pavements is to use dowel bars that are between 19 and 32 mm (0.75 to 1.25”) in diameter and 457 mm (18”) long (Snyder 2011). It was expected that a larger diameter, longer length, and higher un-greased surface would have reduced deflections. Economic issues, placement challenges, and increased stresses from high friction bonds have led the industry to restrict the dimensions to smaller diameters and

standardized lengths, with greased dowels for more slippage of the dowel during loading. Underneath the slabs is a 50 mm-thick (2") Hot Mix Asphalt (HMA) layer followed by a tied 370 mm-thick binder course. A separate cohesive zone was defined between the concrete overlay pavement and underlying HMA layer. The subgrade was idealized as an elastic foundation that only supports compression. An initial notch at the joint location was 3 mm wide and 12 mm deep to simulate a constructed saw-cut. The modeling boundary was simplified to focus on the top overlay joint and interface behavior rather than considering strains or loading distributed through the entire pavement structures.

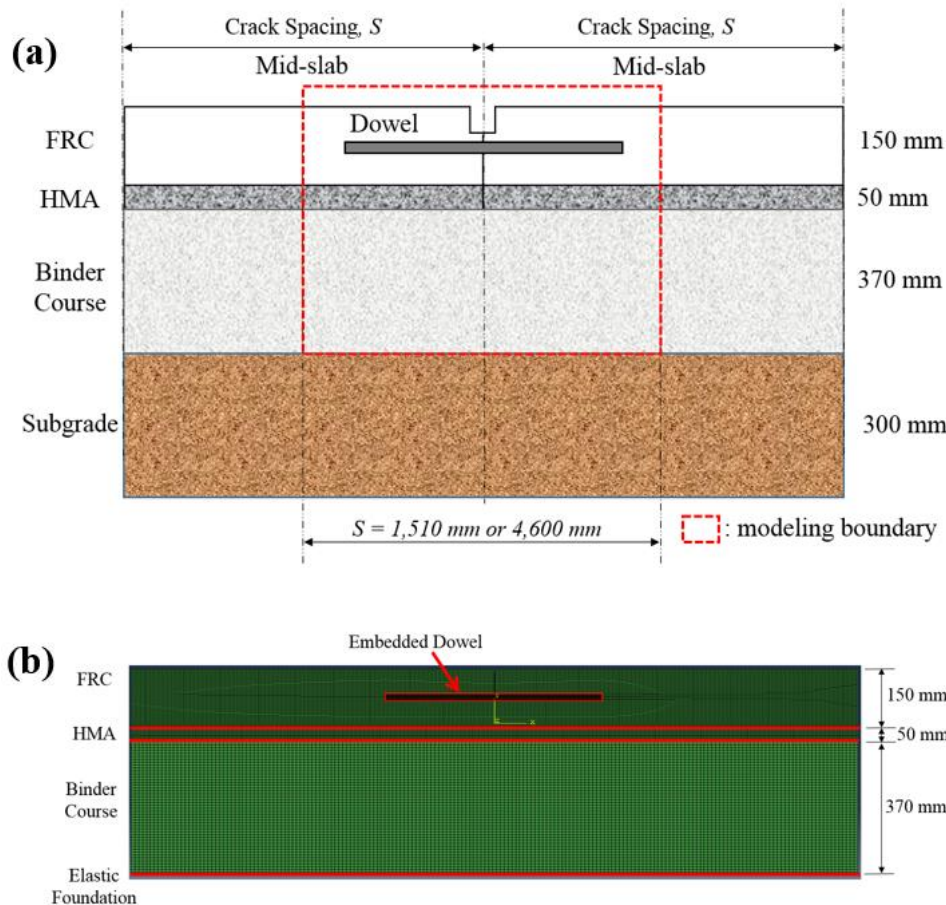


Figure 3.11 Diagrams for (a) the 2D model boundaries; (b) finite element mesh.

Table 3.5 summarizes defined material and interface properties in the model. The dowel was modeled to be low-carbon steel with isotropic linear elastic properties (Levy 2010). The same linear traction-separation cohesion fracture energy from Section 0 was applied in this model. A 0 N/m of fracture energy was applied to simulate a pre-cast zero tensile bond cohesion at the joint vertical interface compared to an estimated 3500 N/m was utilized for FRC full cohesion across the joint.

Table 3.5 Applied Material and Fracture Properties for FEM

Layer	Material Property	Value
Top Layer: PCC* or FRC	Density (kg/m ³)	2313
	Elastic Modulus (GPa)	31.7
	Poisson's ratio	0.15
	Coefficient of thermal expansion (/°C)	10 x 10 ⁻⁶
	Fracture energy (N/m)	0 or 3000
HMA	Density (kg/m ³)	2300
	Elastic Modulus (GPa)	2.75
	Poisson's ratio	0.30
Binder Coarse	Density (kg/m ³)	1900
	Elastic Modulus (GPa)	0.3
	Poisson's ratio	0.35
Dowel	Density (kg/m ³)	7800
	Elastic Modulus (GPa)	200
	Poisson's ratio	0.30
	Coefficient of thermal expansion (/°C)	12 x 10 ⁻⁶
Cohesive Interfaces	Interface Property	Value
Joint with Pre-cast cohesion	Penalty stiffness (Pa/m)	1 x 10 ¹²
	Fracture energy (N/m)	80
	Tensile strength (MPa)	2.0
Joint with FRC full cohesion	Penalty stiffness (Pa/m)	1 x 10 ¹²
	Fracture energy (N/m)	3500
	Tensile strength (MPa)	2.0
Overlay-HMA interface	Penalty stiffness (Pa/m)	1 x 10 ¹²
	Fracture energy (N/m)	70
	Tensile bond strength (MPa)	0.5

* In this case the plain concrete (PCC) material was assumed to have a worst-case scenario of zero fracture energy, such as a pre-cast panel might have.

The contact between dowel and concrete was modeled as a hard contact in ABAQUS with friction between the two separate materials. The contact was defined using a modified friction coulomb response, as shown in Figure 3.12. Khazanovich et al. proposed this modified coulomb method to analyze other dowel-concrete interactions in pavements (Khazanovich et al. 2001). The same authors suggested that a friction coefficient of 0.3 and shear strength of 2.1 MPa adequately described the interface between an epoxy-coated, stainless steel, or low-carbon steel dowel and the surrounding plain concrete (Khazanovich et al. 2009). A lower friction coefficient, listed in Table 3.6, represents a more practical lubricated dowel in concrete.

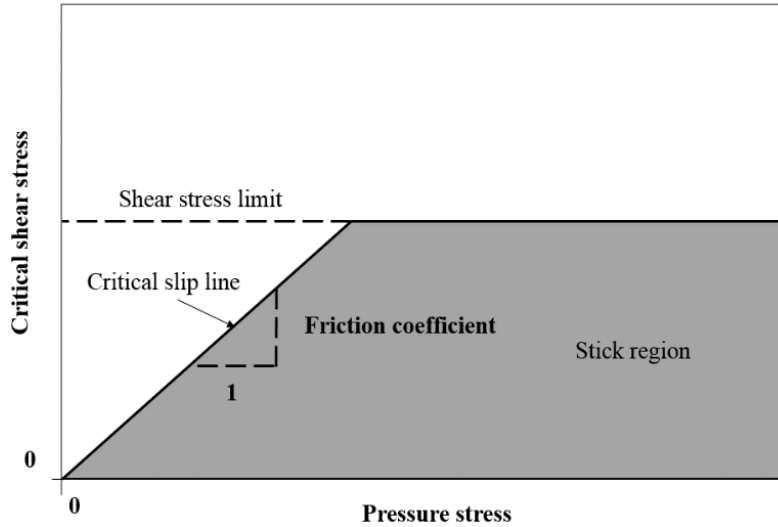


Figure 3.12 Modified coulomb model (Khazanovich et al. 2001).

Table 3.6 Friction Coefficients Between Dowel and Concrete
[from (Khazanovich et al. 2001)]

Uncoated	0.383736
Silicon (greased) coated	0.092568
Tectyl (lubricant) coated	0.076293

3.5.2 Comparison of Plain versus FRC in 150 mm overlay

Figure 3.13(a), (b), and (c) show stress distributions in a 150 mm-thick (6”) overlay of either plain concrete without fibers or dowels, a fiber reinforced concrete, and a PCC overlay with a dowel bar, respectively. As the pavement is subjected to a positive temperature gradient of 20 °C (resembling daytime temperature curling), in all cases, tensile opening of the joint near the top is first seen, followed by different patterns in the stress fields as the crack reaches the interface of the HMA layer below or the dowel bar at the mid-overlay height. Similar to the response of the 50 mm overlay (Section 3.3), some debonding of the PCC or even FRC can be seen directly under the joint location. For the dowel bar without lubrication [Figure 3.13(c)], the finite element analysis predicts a zone of compression or shear is induced in the upper half of the overlay caused from the bearing of the steel dowel against the concrete.

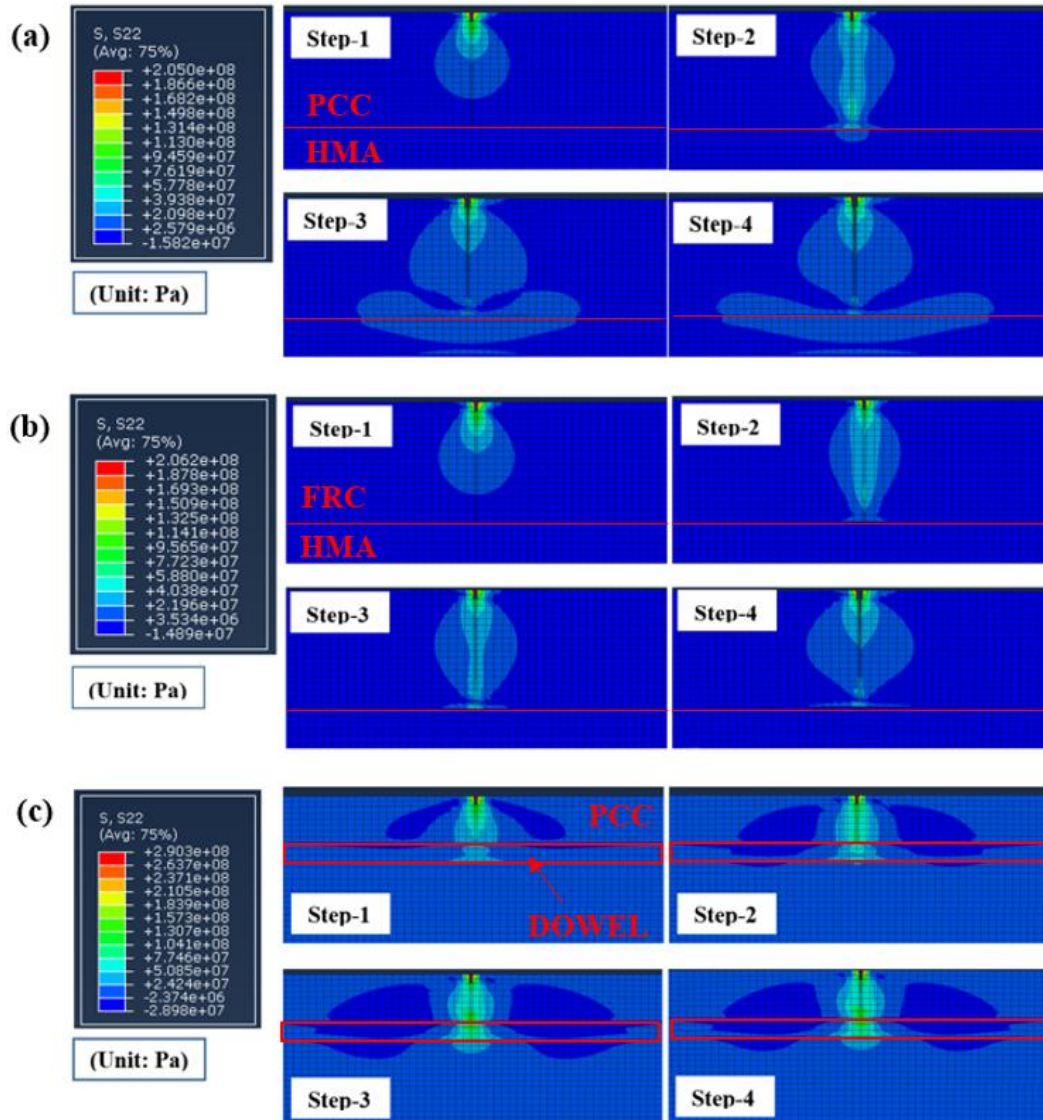


Figure 3.13 Zoomed in stress distribution during cracking and debonding for (a) PCC without dowel; (b) FRC without dowel; (c) single dowel bar model ($\phi = 25$ mm dowel bar, 457 mm long, 0.38 high friction coefficient) in PCC.

Crack widths, debonding lengths, and vertical deflections for either a 1.51m (5 ft.), or a 4.60 m (15 ft.) slab size are shown in Table 3.7 and Table 3.8, respectively. All of the un-doweled simulations predicted that the interface between the overlay and the underlying HMA became debonded. Greased or lubricated dowels in short slabs also showed debonding tendencies. In a plain concrete of zero load, transfer across a joint was verified to have the widest joint opening (seen as crack width) and to have the most debonding at about 5.5% of the interface length, regardless of slab size. Use of fiber reinforced concrete in even the 150 mm thick overlay reduced crack width by a factor of 1.3 times compared to the plain concrete. This is similar to the 1.4 times reduction found in the crack width for a 50 mm thick overlay of FRC. Dowel bars alone were more effective than fiber-reinforcement to reduce crack widths. In this study, implementation of a dowel bar reduced crack widths by 4.3 times compared to unreinforced plain concrete. The combination of a dowel bar with FRC only provided a slight additional reduction of crack width by 1.2 times compared to the dowel model without FRC.

Table 3.7 Result of sensitivity analysis for 1.51 m (5 ft.) slab

Dowel Diameter			
Zero Cohesion (Precast)			
(Unit: mm)	No dowel	19 mm (3/4")	25 mm (1")
Crack Width	0.5113	0.2114	0.1511
Debonding Length	79.8942	0	0
Vertical Deflection	0.1610	0.0905	0.0503
FRC			
(Unit: mm)	No dowel	19 mm (3/4")	25 mm (1")*
Crack Width	0.3758	0.1463	0.1323
Debonding Length	47.9366	0	0
Vertical Deflection	0.1173	0.0347	0.0290
Friction Coefficient			
(Unit: mm)	0.383736	0.092568	0.076293
Crack Width	0.1323	0.2914	0.6827
Debonding Length	0	84.2462	86.3829
Vertical Deflection	0.0290	0.0781	0.0821
Dowel Bar Length			
(Unit: mm)	200 mm (8")	450 mm (18")	700 mm (28")
Crack Width	0.1520	0.1323	0.1142
Debonding Length	0	0	0
Vertical Deflection	0.0291	0.0290	0.0287

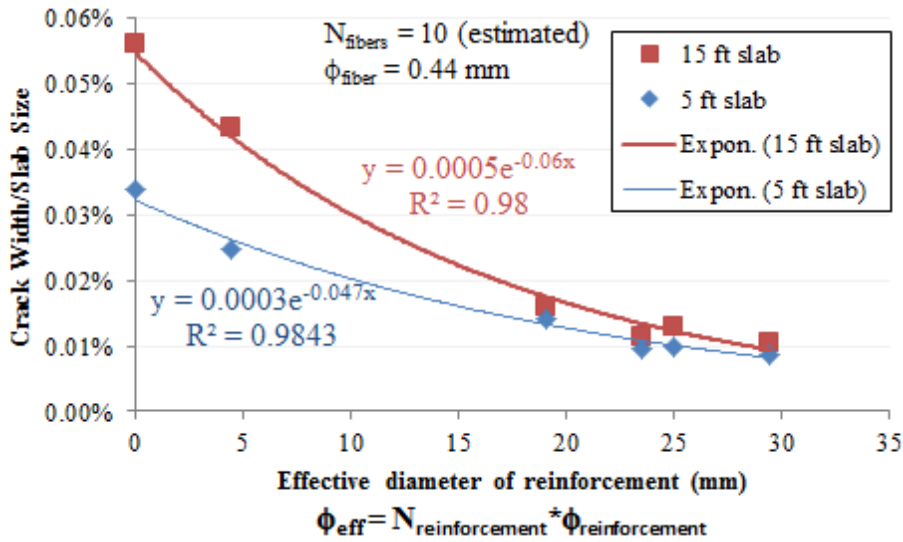
*default settings for other simulations

Table 3.8 Result of sensitivity analysis for 4.60 m (15 ft.) slab

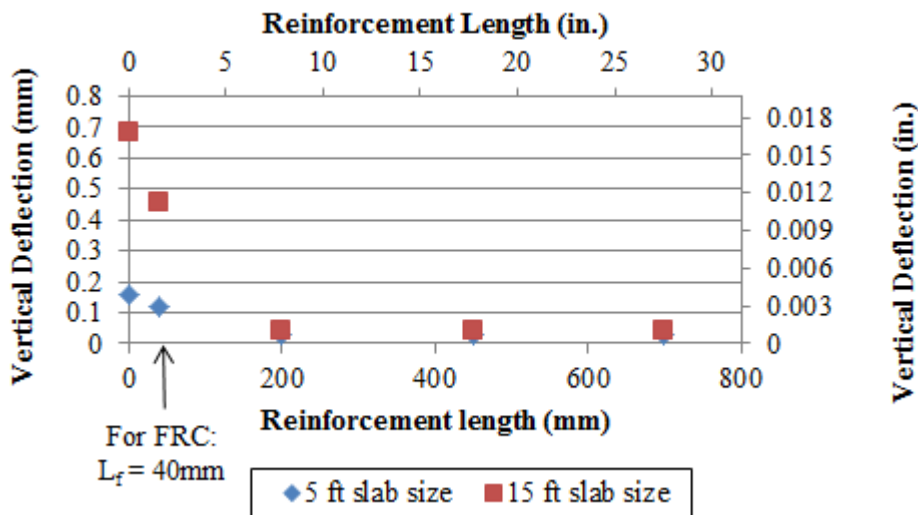
Dowel Diameter			
Zero Cohesion (Precast)			
(Unit: mm)	No dowel	19 mm (3/4")	25 mm (1")
Crack Width	2.56515	0.73291	0.59605
Debonding Length	255.556	0	0
Vertical Deflection	0.68534	0.06712	0.04470
FRC			
(Unit: mm)	No dowel	19 mm (3/4")	25 mm (1")*
Crack Width	1.97767	0.52783	0.48532
Debonding Length	95.833	0	0
Vertical Deflection	0.45662	0.04568	0.04263
Friction Coefficient			
(Unit: mm)	0.383736	0.092568	0.076293
Crack Width	0.48532	0.710582	2.28571
Debonding Length	0	287.5	306.1
Vertical Deflection	0.04263	0.051	0.052
Dowel Bar Length			
(Unit: mm)	200 mm (8")	450 mm (18")	700 mm (28")
Crack Width	0.58915	0.48532	0.43158
Debonding Length	0	0	0
Vertical Deflection	0.04124	0.04263	0.04250

*default settings for other simulations

Figure 3.14 is meant to take an initial step at comparing fibers and dowel bars together as if they were equivalent types of reinforcement, just at different lengths, and cover a different amount of the cross-sectional area. The number of fibers that cross the joint is highly variable and can depend mainly on dispersion during placement and volume fraction. For this simple step, it was assumed that approximately 10 fibers may be found per unit area in FRC (Bordelon and Roesler 2014). Figure 3.14(a) shows that as the net amount of reinforcement increases, the FEM analysis using even total fracture energy to predict FRC can closely predict net effect on the reducing crack width. When length of the reinforcement goes beyond at least 200 mm, there is little additional effect or further reduction of vertical deflections in this equivalent environmental loading.



(a)



(b)

Figure 3.14 (a) Crack widths/slab size and (b) vertical deflections for different amounts of total reinforcement.

An increase in friction coefficient between the dowel and surrounding concrete showed a decrease in w , L_{deb} , and δ_{lift} . The highest friction coefficient for an un-lubricated dowel indicated that compressive stresses develop in the upper half of the concrete overlay and the HMA interface no longer exhibits debonding. A simulation with a fully-lubricated dowel on both ends, shown in Figure 3.15, has a similar stress field response in the upper half of the overlay as the stress field for the 50 mm overlay of plain concrete. In the case of the lubricated dowels, the FEM indicated that there may be separation and lift-off of the upper-portion of the concrete slab from the dowel when subjected to an environmental load.

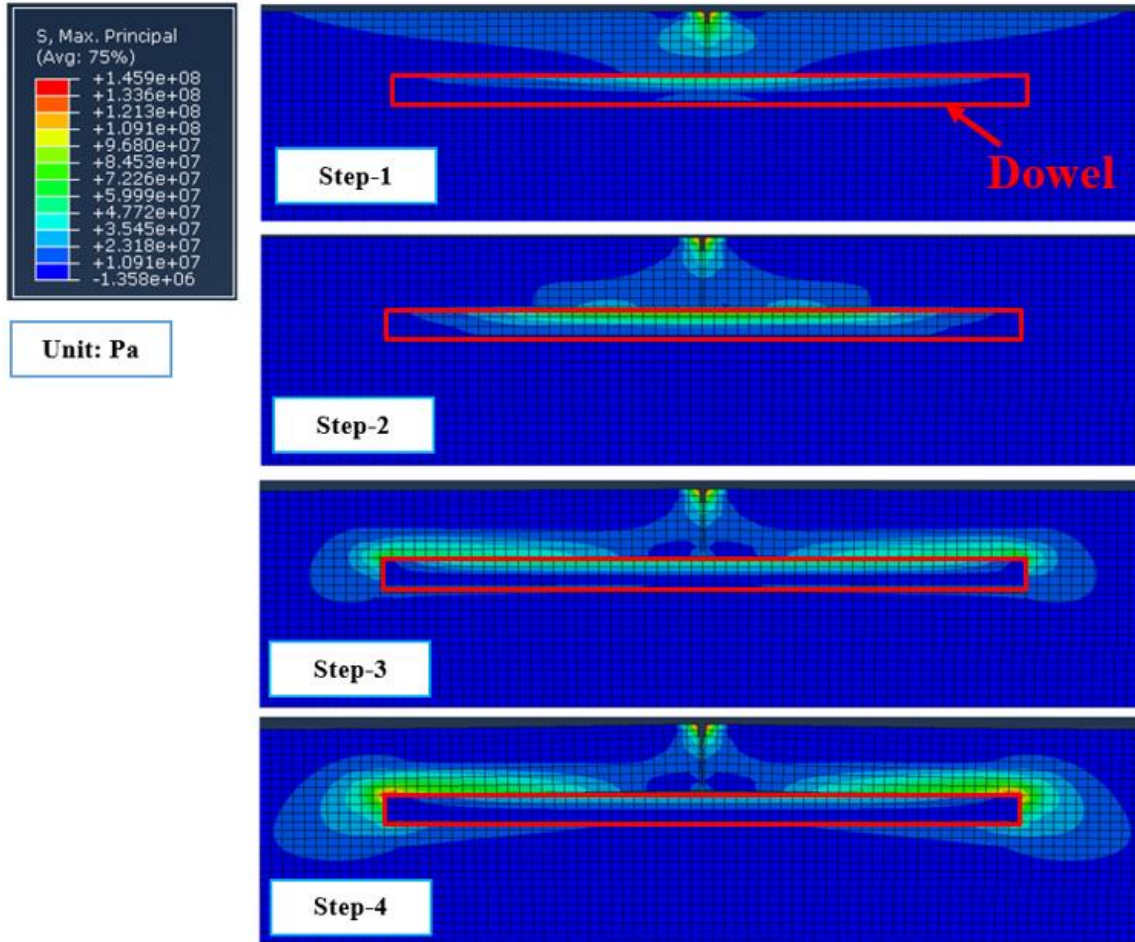


Figure 3.15 Zoomed in stress distribution during cracking of dowelled FRC overlay with the lowest friction coefficient shows separation of concrete from dowel at joint location.

3.6 FEM Findings

A simple finite element model was developed to analyze effects of the high FRC total fracture energy and implementation of dowel reinforcement at the joint on crack width, vertical deflection, and debonding length in an overlay. The FEM was designed to represent different slab sizes from 50 mm or 150mm thickness and from 1.12 m to 4.6 m joint spacing. An equivalent environmental (shrinkage and temperature loading) was applied for all simulations so some could be compared against data from an environmentally-loaded field FRC overlay of similar dimensions and material properties.

Fiber-reinforcement and dowel reinforcement both reduced the crack widths, vertical deflections, and HMA interfacial debonding, as shown in the FEM. Although dowels are more effective than FRC in 150 mm thick pavements, for the limited thickness of a 50 mm overlay, the FRC is a recommended option. Even if a 50 mm (2 in.) overlay was constructed with large joint spacing (such as 3.35 m or 11 ft), the crack width was reduced by 11% with the use of FRC compared to plain concrete. The FEM also was used to verify that even with FRC in a 50 mm overlay, a soft subgrade of 50 kPa/mm or high tensile bond strength of 2.5 MPa could also produce a low crack width, vertical deflection, and debonding length.

4. FIBER EFFECT ON INTERFACIAL BOND BETWEEN CONCRETE AND FIBER REINFORCED MORTAR

4.1 Introduction

Bond properties between the old substrate and FRC overlay are assumed to be unaffected by the addition of fibers, yet field studies and the FEM study indicate that curling and debonding length is reduced with the addition of fibers. In this regard, this portion of the research focused on verifying whether adding fibers in the new overlay concrete affected the measured interfacial bonding properties. This section explores whether interfacial bond properties change between an aged concrete substrate and a new overlay with the addition of common fiber types and reasonable volume contents. Tensile and shear bond strength at the interface between concrete and fiber reinforced mortar (FRM) are measured.

4.2 Experimental Investigation

4.2.1 Materials and Test Variables

Three different types of fibers (described in Table 4.1) and two different dosage rates for each fiber were considered in this study. The volume fraction dosage rates of the fibers were 0.40% and 0.78% for a slender and long polymeric fiber (Y1), 0.5% and 1.0% for a long polymeric fiber (Y2), and 1.0% and 2.0% for a short steel fiber (T). These fiber types and respective dosage rates were selected to represent potential applications of slabs-on-ground, overlays, and bridge decks. Short steel fibers were expected to produce the highest tensile fracture resistance, and long polymeric fibers were expected to have a slightly higher tensile performance than the slender and long polymeric fibers (Bordelon 2007).

Table 4.1 Properties of Fibers

Fiber Type	Slender and Long Polymeric (Y1)	Long Polymeric (Y2)	Short Steel (T)
Material	Polypropylene-polyethylene	Polypropylene	Steel
Cross section	Rectangular	Rectangular	Circular
Length	40 mm (1.6 in.)	50 mm (2.0 in.)	33 mm (1.3 in.)
Diameter	-	-	0.55 mm (0.02 in.)
Thickness	0.105 mm (0.004 in.)	0.4 mm (0.016 in.)	-
Width	1.4 mm (0.06 in.)	1.2 mm (0.05 in.)	-
Aspect ratio	90	75	60
Specific gravity	0.92	0.91	7.85
Tensile strength	620 MPa (90 ksi)	550 MPa (80 ksi)	1300 MPa (189 ksi)
Modulus of elasticity	9.5 GPa (1378 ksi)	7.0 GPa (1015 ksi)	210 GPa (30458 ksi)

The mortar mixture proportions of those fiber materials are shown in Table 4.2. The mortar mixture was based on a FRM design with a reported good workability for higher fiber contents > 0.5% (Sevil et al. 2011). The original substrate material was made as a concrete with the mixture design listed in Table 4.2.

Table 4.2 Mix Design for Substrate Concrete and Fiber Reinforced Mortars

Material		Substrate Concrete	Control Mortar	Slender and Long Polymeric (Y1) Mortar	Long Polymeric (Y2) Mortar	Short Steel (T) Mortar
Water		187 kg/m ³ (315 pcy)	330 kg/m ³ (556 pcy)			
Type I/II Cement		468 kg/m ³ (788 pcy)	579 kg/m ³ (975 pcy)			
Coarse Aggregate		1052 kg/m ³ (1773 pcy)	0			
Fine Aggregate		857 kg/m ³ (1445 pcy)	1592 kg/m ³ (2684 pcy)			
Polycarboxylate High Range Water Reducer		1028 mL/m ³ (26.4 fl.oz./yd ³)	880 mL/m ³ (22.6 fl.oz./yd ³)			
Air Entraining Admixture		107 mL/m ³ (2.7 fl.oz./yd ³)	0			
Fiber	(for low volume fraction)	0	0	3.6 kg/m ³ (6.1 pcy)	4.5 kg/m ³ (7.6 pcy)	79 kg/m ³ (133 pcy)
	(for high volume fraction)			7.2 kg/m ³ (12.2 pcy)	9.0 kg/m ³ (15 pcy)	157 kg/m ³ (266 pcy)

This original substrate contained limestone coarse aggregates of 9 mm maximum aggregate size. All mixtures contained fine aggregates that were natural sand. The substrate concrete specimens were moist-cured at a relative constant temperature of 30 °C (86 °F) for 28 days prior to new overlay construction. All aged substrate samples were sandblasted prior to constructing new overlay mortar. Table 4.3 summarizes the sample labelling nomenclature based on tested variables of loading type, fiber type, and fiber volume contents.

Table 4.3 Test Variables

Specimen	Stress	Fiber Type	Fiber Content	Specimen	
TM-0 (Control)	Tensile	NONE	-	Monolithically-cast Fiber Reinforced Mortar	
TM-Y1-L		Slender and Long Polymeric	Low (0.40%)		
TM-Y1-H			High (0.78 %)		
TM-Y2-L		Long Polymeric	Low (0.50%)		
TM-Y2-H			High (1.0%)		
TM-T-L		Short Steel	Low (1.0%)		
TM-T-H			High (2.0%)		
TH-0 (Control)		Tensile	NONE	-	Composite (Half Concrete Substrate + Half Fiber Reinforced Mortar)
TH-Y1-L			Slender and Long Polymeric	Low (0.40%)	
TH-Y1-H				High (0.78 %)	
TH-Y2-L			Long Polymeric	Low (0.50%)	
TH-Y2-H				High (1.0%)	
TH-T-L			Short Steel	Low (1.0%)	
TH-T-H				High (2.0%)	
SH-0 (Control)	Shear	NONE	-	Composite (2/3 Concrete Substrate + 1/3 Fiber Reinforced Mortar)	
SH-Y1-L		Slender and Long Polymeric	Low (0.40%)		
SH-Y1-H			High (0.78 %)		
SH-Y2-L		Long Polymeric	Low (0.50%)		
SH-Y2-H			High (1.0%)		
SH-T-L		Short Steel	Low (1.0%)		
SH-T-H			High (2.0%)		

4.2.2 Bulk Material Property Tests

Each mixture was tested for bulk material properties for consistency, including fresh workability, compressive strength, and split tensile strength. For workability, the concrete mixture was tested for slump flow (ASTM C1611), while mortar mixtures were tested with a mini-slump test (ASTM C1437). Compressive strength (ASTM C39 and ASTM C109) was performed using 100×200 mm (4×8 in.) cylinders for the substrate concrete, or using 50 mm (2 in.) cubes for the mortar mixtures, respectively. All split tensile strengths (ASTM C496) were measured based on 100×200 mm (4×8 in.) cylinders regardless of whether it was concrete or mortar. Fracture properties of the concrete and mortar mixtures were determined using a wedge split tension 150 mm (6 in.) cube samples similar to that shown in Figure 4.1 and described later.

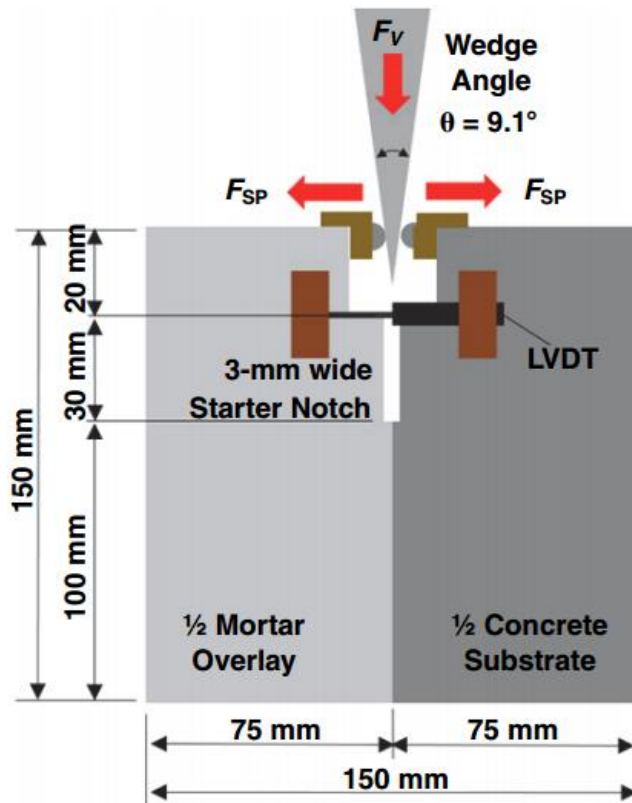


Figure 4.1 Interfacial wedge splitting tension test configuration and LVDT mounting.

4.2.3 Composite Sample Fabrication

The size of the substrate concrete for the wedge split test was 150×150×75 mm (6×6×3 in.) and for the bi-surface shear test was 150×150×50 (6×6×2 in.). Sandblasting, in combination with power-washing, was found to be the best method by other researchers to create a rough textured interface similar to field milling (Momayez et al. 2004; Tayeh et al. 2012). The procedure to age and roughen the surface prior to casting the mortar overlay follows:

1. Styrofoam inserts were placed in mold to occupy space of future overlay material, and an insert used for the roller assembly location for wedge split specimens.
2. Substrate concrete was cast.
3. At 24 hrs from casting, the substrate concrete was demolded and placed in fog room.
4. Within three days of casting, substrate concrete was sandblasted and power-washed, then placed back in fog room.
5. An hour prior to full 28 days cure, contact surface was wiped dry with paper towel for saturated surface dry condition.
6. The aged substrate concrete was placed back in the mold, with the same styrofoam insert for the roller assembly for the wedge split specimens.
7. The mortar mixture was cast.
8. At 24 hrs from mortar casting, composite mortar-concrete was demolded and placed in water bucket for 28 days.
9. At the test date, a starter notch was cut in the composite sample for the wedge split specimens. For the bi-surface shear specimens, a guide notch was cut along the side of the samples.

4.2.4 Wedge Split Tension Test

As listed in Table 4.1, both monolithically-cast mixtures and the composite FRM overlay cast against the substrate concrete were tested with the wedge split tension cube test. The applied vertical load and two opening displacements were measured. From the load versus displacement curve, the tensile bond strength, fracture energy for bond, and crack growth resistance are calculated (Hillerborg 1985; Tschegg 1991). Two replicate specimens were produced for each wedge split test configuration. The applied vertical force F_V load transmits through a slender wedge of total angle θ and low friction coefficient f roller assembly into a splitting force F_{SP} . This horizontally splitting force F_{SP} can be calculated according to Eq. (4.1). The test was conducted with a constant vertical loading rate of 1 mm/min (0.04 in./min).

$$F_{SP} = \frac{F_V}{\tan \theta} \frac{1-f \tan \theta}{1+f \cot \theta} \approx \frac{F_V}{2(1+f \cot \theta) \tan \theta} \quad (4.1)$$

Two linear variable differential transformers (LVDTs) were in line with the notch tip location and clamped against the specimen with a custom-built frame. The recorded average displacement was used to calculate the crack opening displacement (COD). For monolithically-cast specimens, a cut-off total fracture energy was computed based on the load versus displacement area until the COD reached 2.5 mm (0.1 in.) as shown in Eq. (4.2).

$$G_{2.5mm} = \frac{area(F_{SP} \cdot COD)|_{COD=2.5}}{A} \quad (4.2)$$

where *area* is the sum of the area under the horizontal load F_{SP} versus COD curve, and A is the fracture cross-sectional area ahead of the notch tip (15000 mm² or 23.3 in.²).

For the half-cast interfacial specimens, a similar fracture energy for the interface bond (G_{bond}) was computed based on the load-displacement area, until the first failure occurred, as seen in Eq. (4.3).

$$G_{bond} = \frac{area(F_{SP} \cdot COD)}{A} \quad (4.3)$$

4.2.5 Bi-Surface Shear Test

Figure 4.2 shows the geometry and loading of the bi-surface shear specimen. The test was conducted with a constant loading rate of 1 mm/min (0.04 in./min). Two LVDTs were attached to estimate shear displacement on both front and back faces of the specimen. The test was determined complete when failure occurred at the interface. The shear bond strength, f_s from Eq. (4.4) is calculated by dividing the load at failure P_P by the original bonded area A (15000 mm² or 23.3 in.²).

$$f_s = \frac{P_P}{A} \quad (4.4)$$

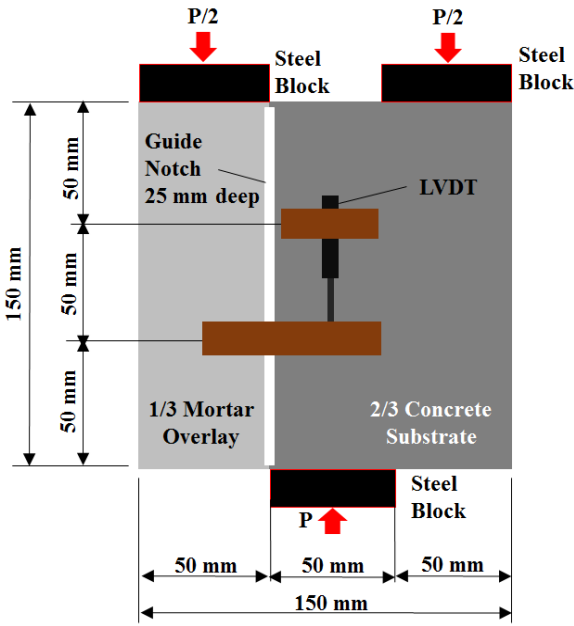


Figure 4.2 Bi-surface shear test configuration.

4.3 Experimental Results and Discussion

4.3.1 Bulk Properties

The averaged compressive strengths of the mortar mixtures are shown in Table 4.4 based on three specimens each at 7 days and 28 days. As shown from the list of p-values in Table 4.5, no significant trend could be found with the addition of fibers on the compressive strength of the mortar. However, an additional strength test for the split tensile strength of the mortar mixtures did find that the FRM was higher with a 97% confidence than that of control mortar; and the tensile strength increased as fiber volume content increased.

Table 4.4 Fresh and Hardened Properties of Concrete and Fiber Reinforced Mortar

Type	Slump Flow	Compressive Strength, 7 days		Compressive Strength, 28 days		Split Tensile Strength, 28 days	
	Concrete, mm Mortar, %	MPa [psi]	COV (%)	MPa [psi]	COV (%)	MPa [psi]	COV (%)
Substrate Concrete	508	N/A	N/A	60.7 [8804]	0.6	3.9 [566]	8.0
Control Mortar	125	22.9 [3321]	9.9	30.6 [4438]	9.5	2.1 [305]	18.7
Y1 – 0.40%	N/A	24.4 [3533]	5.8	26.9 [3902]	11.1	2.7 [392]	3.2
Y1 – 0.78%	N/A	18.7 [2712]	11.9	29.9 [4337]	5.9	2.8 [406]	8.5
Y2 – 0.5%	129	23.3 [3379]	2.0	26.6 [3858]	10.3	3.4 [493]	2.4
Y2 – 1.0%	135	20.5 [2973]	10.6	30.7 [4453]	3.3	3.5 [508]	9.2
T - 1.0%	131	26.8 [3887]	8.6	32.0 [4641]	13.3	3.7 [537]	8.1
T - 2.0%	133	25.4 [3684]	10.7	30.3 [4395]	4.5	3.9 [566]	4.1

Note: all strength values are an average of three samples. Slump values are recorded once for each mixture.

Table 4.5 Calculated P-Values Between Control Mortar versus FRM Mixture Strengths

	Compressive Strength, 7 days	Compressive Strength, 28 days	Split Tensile Strength, 28 days
Y1 – 0.40%	0.496	0.281	0.0002
Y1 – 0.78%	0.135	0.787	0.016
Y2 – 0.5%	0.844	0.226	0.002
Y2 – 1.0%	0.340	0.983	0.027
T - 1.0%	0.168	0.719	0.003
T - 2.0%	0.368	0.879	0.004

Note that for a level of significance of 0.05, a p-value less than this value verifies that the sample mixtures are not the same.

Table 4.6 lists fracture properties and Figure 4.3 shows splitting force versus crack opening displacement curves for monolithically-cast mortar specimens. The split-tensile strength indicated no significant trend (see Table 4.7) from the addition of fibers to the mortar. As expected, an increase in fiber volume content among mortar fracture specimens did result in an increase in the post-cracking performance. The cut-off fracture energy was again found to slightly decrease for the larger aspect ratio fibers, despite the more dominant effect of the increasing volume content on fracture energy.

Table 4.6 Results for Monolithically-Cast Wedge Splitting Mortar Samples

Specimen	F _{SP,MAX}			G _{2.5mm} *			F _{SP,2.5mm}		
	(kN)	(kip)	COV (%)	(N/m)	(lb/in.)	COV (%)	(kN)	(kip)	COV (%)
TM-0	9.92	2.23	21.4	56.47	0.322	4.0	0	0	-
TM-Y1-L	9.12	2.05	0.5	382	2.181	18.5	2.17	0.49	18.7
TM-Y1-H	11.09	2.49	8.6	606	3.460	18.9	2.65	0.60	19.0
TM-Y2-L	10.83	2.43	1.2	607	3.466	8.2	4.13	0.93	24.2
TM-Y2-H	9.23	2.07	16.2	1117	6.378	8.6	6.90	1.55	11.3
TM-T-L	10.59	2.38	5.6	1222	6.978	10.4	5.25	1.18	13.2
TM-T-H	-								

Note: all wedge split test result values are an average of two samples.

*Total fracture energy of the un-reinforced mortar fails before the 2.5 mm cut-off.

Table 4.7 P-values for Monolithically-Cast Splitting Tensile Force

	Splitting Force, F _{SP,MAX}
TH-Y1-L	0.771
TH-Y1-H	0.703
TH-Y2-L	0.743
TH-Y2-H	0.817
TH-T-L	0.901

Note: P value less than 0.05 means not the same.

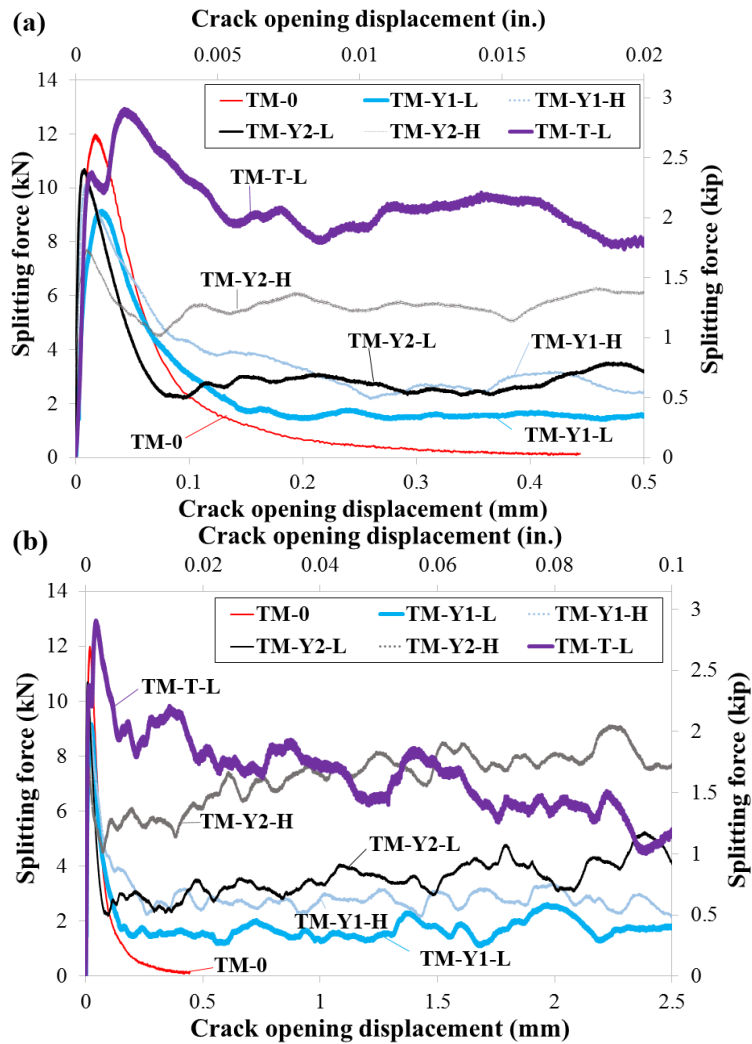


Figure 4.3 Wedge splitting force versus COD curves for one replicate of each monolithically-cast mortar specimens, (a) showing zoomed in; (b) showing full displacement range.

4.3.2 Interface Tensile Splitting Results

Figure 4.4 shows that all composite samples exhibited a sudden drop in load after peak tensile bond strength is reached. For specimens containing FRM, a tensile stress was still carried for more than 0.3 mm COD than for specimens containing the unreinforced mortar. The main difference between Figure 4.3 and Figure 4.4 is that with the monolithically-cast mortar specimens a chemical and physical bond exists across the fracture plane, while the interface composite specimens are expected to only have a macro-texture friction to resist fracture.

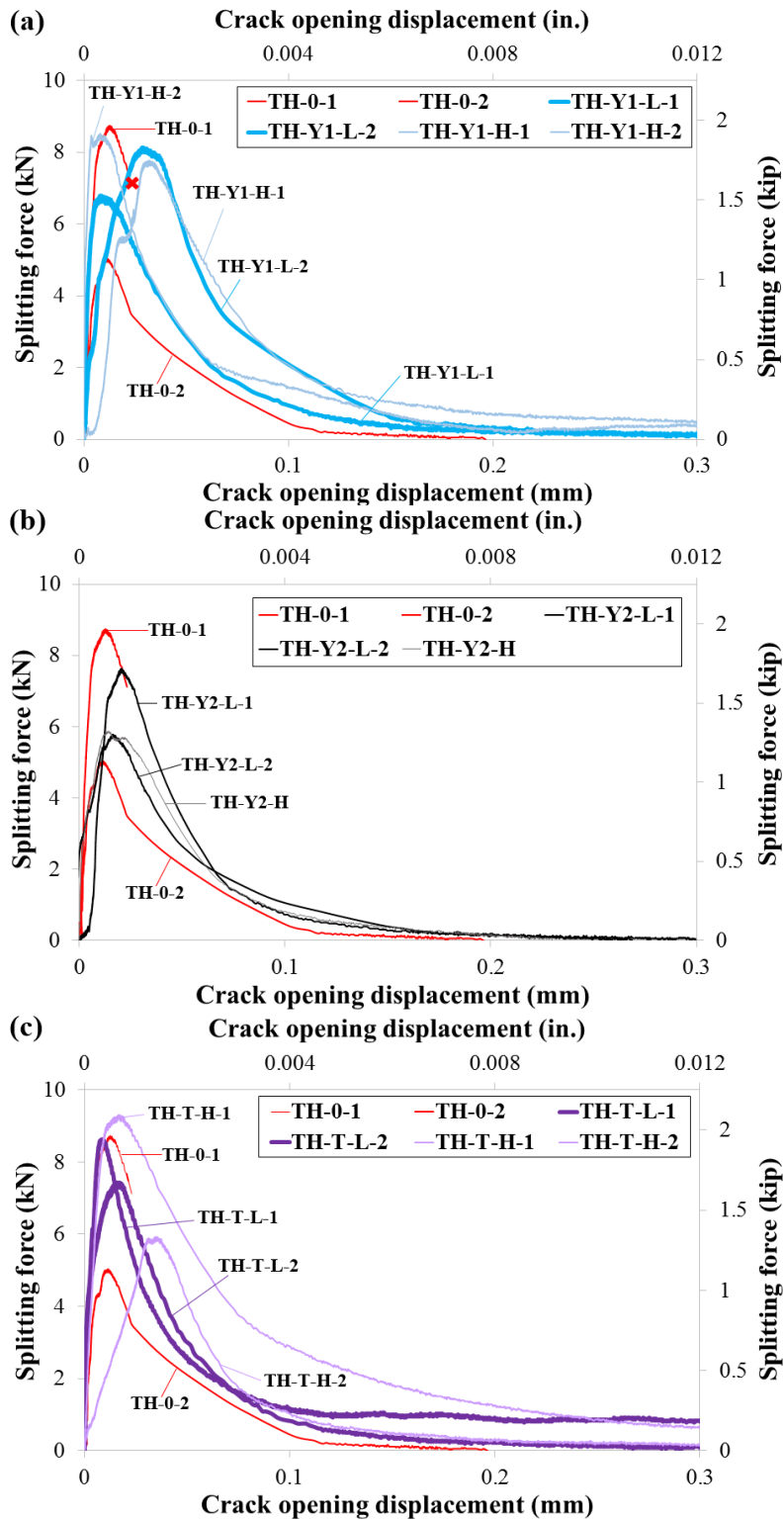


Figure 4.4 Interfacial splitting tension force versus crack opening displacement curves for composite specimens: (a) 1/2 concrete + 1/2 slender and long polymeric FRM; (b) 1/2 concrete + 1/2 long polymeric FRM; (c) 1/2 concrete + 1/2 short steel FRM.

Table 4.8 shows peak tensile strength, $F_{SP,MAX}$ and fracture energy for the interfacial tensile bond based on wedge split composite specimens. Again, using a t-test two-tailed statistic, the p-values, as shown in Table 4.9, indicate no significant trend could be found on the peak interfacial tensile load or interfacial bond energy from the addition of fibers.

Table 4.8 Results for Bonded Composite ½ Concrete + ½ Mortar Samples

Specimen	$F_{SP,MAX}$			G_{bond}			# of fibers through fracture area
	(kN)	(kip)	COV (%)	(N/m)	(lb/in.)	COV (%)	
TH-0	6.89	1.55	26.9	13.60	0.078	18.4	-
TH-Y1-L	7.46	1.68	9.0	33.18	0.189	20.5	8
TH-Y1-H	8.15	1.83	4.6	79.82	0.456	16.8	45
TH-Y2-L	6.71	1.51	13.8	24.24	0.138	1.3	4
TH-Y2-H	5.87	1.32	-	23.46	0.134	-	9
TH-T-L	8.03	1.81	8.0	69.25	0.395	5.8	30
TH-T-H	7.61	1.71	22.2	70.70	0.404	6.4	35

Note: all wedge split test result values are an average of two samples.

Table 4.9 P-values for Bonded Samples

	Splitting Force, F_{SP}	Bond Energy, G_{bond}
TH-Y1-L	0.819	0.225
TH-Y1-H	0.626	0.129
TH-Y2-L	0.945	0.149
TH-Y2-H	0.855	0.420
TH-T-L	0.662	0.400
TH-T-H	0.800	0.427

Note: P value less than 0.05 means not the same.

In this study, an increase in tensile bond energy was found with the addition of fibers, which is not commonly expected since the fibers do not cross the original interface surface. In this experiment, the G_{bond} for the FRM specimens containing slender and long polymeric (Y1), long polymeric (Y2), or short steel (T) fibers at the highest fiber contents were about 5.8, 1.7, and 5.2 times higher, respectively, than that of the unreinforced mortar. The t-test statistic comparing mean values of bond energies between the FRM bonded to concrete versus new un-reinforced concrete bonded to concrete. However, a regression plot shown in Figure 4.5 suggests that tensile bond fracture energy does increase with fibers, more specifically to the number of fibers located nearest to the interface.

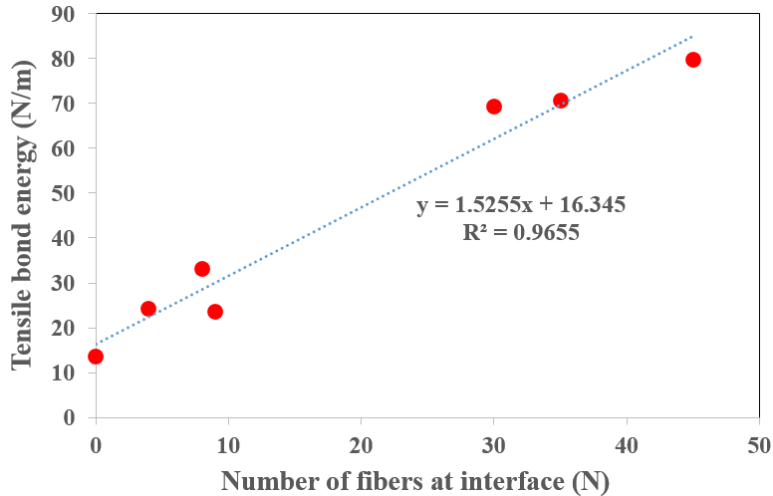


Figure 4.5 Plot shows the relation between G_{bond} and number of fibers at interface.

A closer look at the fractured surface of these composite wedge specimens confirms that many of the samples have a tortuous crack which penetrated both the FRM overlay material and the aged concrete substrate material. This clear correlation found (with a 97% confidence) between the number of fibers crossing the fracture plane does not necessarily relate to original fiber volume content, but was still found to relate to the tensile G_{bond} . It was found that FRM specimens containing Y1 or T fibers had roughly 4 to 5 times more fibers crossing the fractured path compared to FRM specimen with Y2 fiber. It is expected that these fibers located in the crack path were the cause of the increased tensile bond energy performance compared to the unreinforced mortar overlay.

4.3.3 Bi-Surface Shear Results

Figure 4.6 shows shear load versus displacement curves of bi-surface shear specimens. All composite specimens exhibited failure promptly after the ultimate shear bond, P_p was reached. On average, most FRM samples exhibited an increased shear bond strength (shown in Table 4.10) compared to unreinforced mortar overlay samples. However, short steel (T) sample at the high fiber content actually showed a significant decrease in shear strength at the interface. Although this test method was selected for producing low variability, the coefficient of variation is still relatively high for many of these samples and therefore no statistical significant trends could be drawn on most samples.

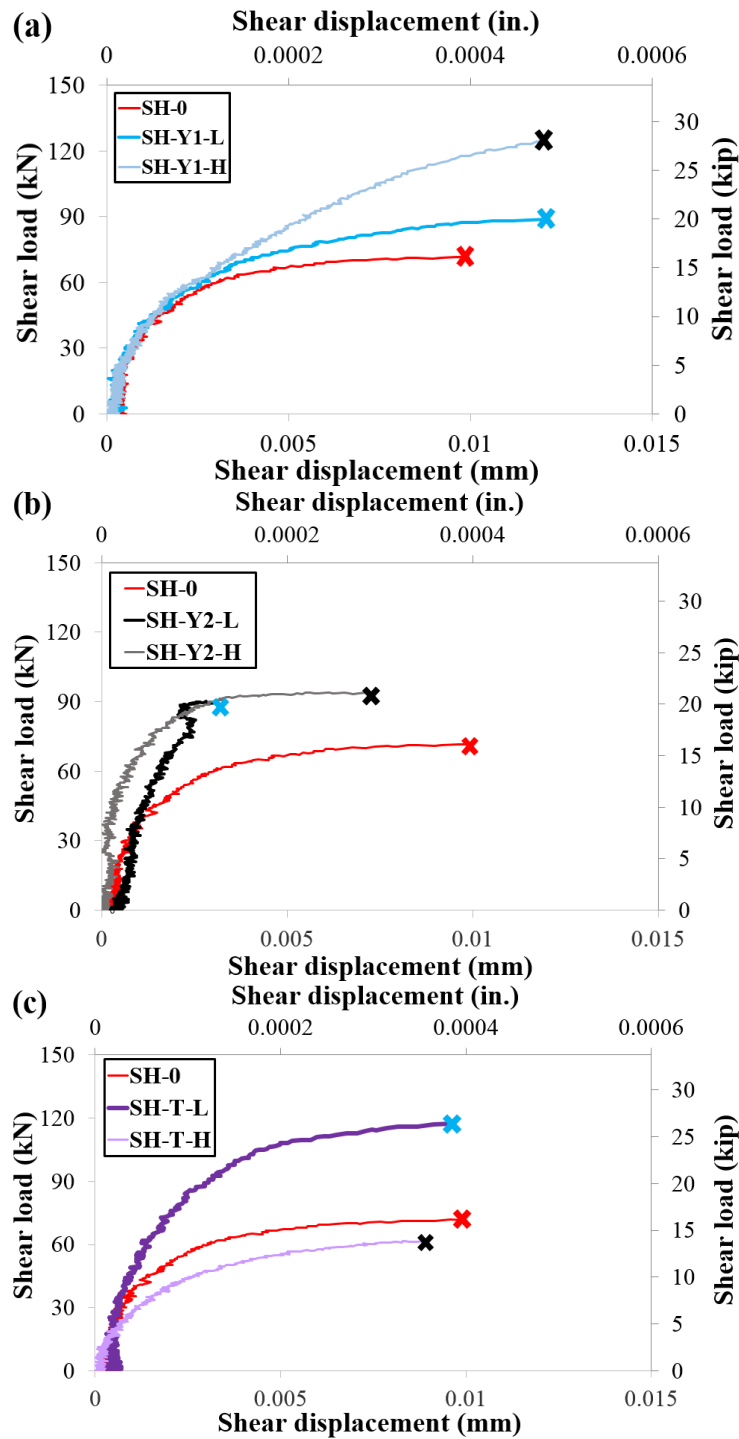


Figure 4.6 Averaged shear load-displacement curves for composite samples: (a) 2/3 concrete+1/3 slender and long polymeric FRM; (b) 2/3 concrete + 1/3 long polymeric FRM; (c) 2/3 concrete + 1/3 short steel FRM.

Unlike to the previous tensile bond energy discovery, number of fibers at the interface of shear specimens (see Table 4.10) was not correlated with the measured shear strength. It is possible that shear bond energy instead of strength might indicate a correlation with fiber content. Although this test method was selected for producing low variability, the coefficient of variation is still relatively high for many of these samples

and therefore no statistical significant trends could be drawn on most samples (see Table 4.11). Also, unlike the previous tensile bond energy discovery, the number of fibers at the interface of these shear specimens (see Figure 4.7) was not correlated with the measured shear strength. Any possible post-cracking response was not captured by the testing apparatus, and thus shear bond energy could not be determined at this time. Further research is needed to understand how fibers could influence the shear interfacial bond performance.

Table 4.10 Results for Bi-Surface Shear Test

Specimen	Shear Load P_P		Shear bond Strength f_s			# of fibers through fracture area
	(kN)	(kip)	(MPa)	(psi)	COV (%)	
SH-0	71.79	16.14	4.79	695	14.4	-
SH-Y1-L	90.15	20.27	6.01	872	9.9	17
SH-Y1-H	124.48	27.98	8.30	1204	1.9	23
SH-Y2-L	81.15	18.24	5.41	785	26.7	2
SH-Y2-H	85.50	19.22	5.70	827	43.5	4
SH-T-L	117.22	26.35	7.81	1133	2.7	18
SH-T-H	62.91	14.14	4.19	608	26.4	35

Note: all bi-surface shear test result values are an average of two samples

Table 4.11 P-Values for Bi-Surface Shear Properties Between Control and FRM

	Shear Load, P_P	Shear Bond Strength, f_s
TH-Y1-L	0.409	0.409
TH-Y1-H	0.177	0.177
TH-Y2-L	0.874	0.874
TH-Y2-H	0.850	0.850
TH-T-L	0.209	0.209
TH-T-H	0.196	0.196

Note: P value less than 0.05 means not the same.

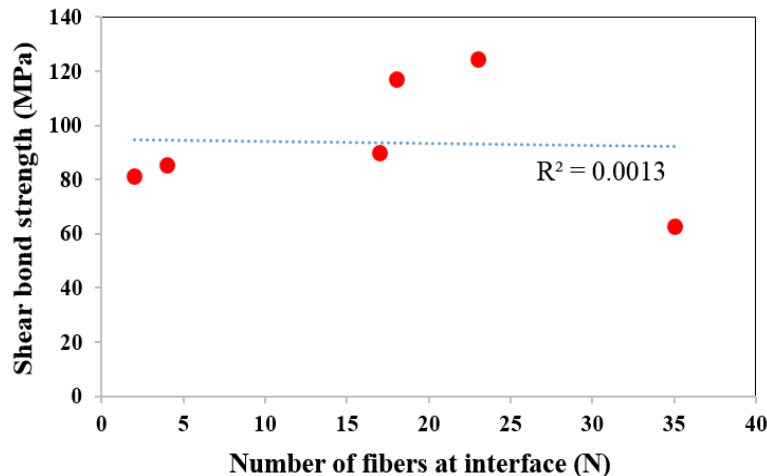


Figure 4.7 Plot shows the relation between f_s and number of fibers at interface.

4.4 Experimental Bond Test Findings

Previous reports of field-constructed FRC overlays indicated that fiber reinforcement may reduce debonding. This section shows the test apparatus built and specimen manufacturing process for experimentally determining tensile and shear bond properties of an overlay material cast against a substrate. The wedge split tension cube test and the bi-surface shear cube test were created to measure these properties because previous research indicated they had low variability in measured properties. Three types of macro-fibers were compared as reinforcement in a mortar overlay mixture, and a single aged portland cement-based concrete mixture was used as the substrate. Based on measured property results, the following conclusions were drawn:

- All of the tested fiber-reinforced mortar mixtures were verified to have a higher split-tensile strength and higher fracture energies compared to un-reinforced mortar.
- A fiber-reinforced mortar, as an overlay against a concrete substrate, was found to have failure through the new overlay, and the number of fibers near the interface was linked to the magnitude of higher interfacial tensile debonding energy.
- Variability in the bi-surface shear test method was still too high (at 44%) to determine statistical trends regarding the effect of fiber-reinforcement on the shear bond properties.

Overall, there is no evidence that the addition of fibers will increase bond properties between the overlay and underlying substrate. The net effect of reduced debonding found in the field is presumed to be linked instead to the reduced crack widths of the higher fracture energy from the FRC. This reduced crack width consequently also is presumed to reduce the curling vertical lift-off seen in field experiments and in the FEM.

5. CONCLUSIONS

This study aimed to investigate how fibers influence on the cracking and debonding of a thin fiber-reinforced concrete overlay subjected to temperature loading. Based on results of experimental and analytical studies, the following conclusions and recommendations can be drawn:

- Overlays with a high fracture energy (such as with FRC), high tensile HMA-overlay bond strength (such as prior milling and cleaning), a low subgrade stiffness, or short slab sizes were all verified to have reduced joint opening widths, reduced debonding lengths, and reduced interfacial vertical lift-off deflections.
- The FEM study revealed that implementing an FRC mixture with a higher fracture energy, more than an optimizable limit, would not provide additional reduction in crack opening, debonding length, or vertical deflection movement. This optimizable limit was found to be dependent on the magnitude of environmental loading and the joint spacing. Other factors may affect optimized FRC fracture energy or toughness properties.
- Fiber-reinforcement appeared to be a promising replacement for dowel bars if there are enough fibers in the joint cross-section or thinner overlays where dowels are impractical.
- The effect of selected macro-fibers on shear bond was not significant. Further experimental approach might be necessary to modify the current test method for bi-surface shear.
- Additional field studies of FRC are recommended for construction and analysis, particularly those subjected to traffic loading, to provide additional data to verify trends seen in the finite element analysis.

REFERENCES

- ABAQUS (2001). *ABAQUS/standard user's Manual*, Hibbitt, Karlsson & Sorensen.
- ACI Committee 544 (1993). "Guide for Specifying, Proportioning, Mixing, Placing, and Finishing Steel Fiber Reinforced Concrete." *ACI Materials Journal*, 90(1), 94-103.
- Balaguru, P., and Ramakrishnan, V. (1988). "Properties of fiber reinforced concrete: workability, behavior under long-term loading, and air-void characteristics." *ACI Materials journal*, 85(3), 189-196.
- Banthia, N., Gupta, R., and Mindess, S. "Developing crack resistant FRC overlay materials for repair applications." *Proc., NSF Conference, Bergamo, Italy*, 99-106.
- Banthia, N., and Sheng, J. (1996). "Fracture toughness of micro-fiber reinforced cement composites." *Cement and Concrete Composites*, 18(4), 251-269.
- Banthia, N., Yan, C., and Mindess, S. (1996). "Restrained shrinkage cracking in fiber reinforced concrete: a novel test technique." *Cement and Concrete Research*, 26(1), 9-14.
- Bordelon, A. (2007). "Fracture behavior of concrete materials for rigid pavement systems." *Masters Thesis*, University of Illinois at Urbana-Champaign.
- Bordelon, A. (2011). "Flowable Fibrous Concrete For Thin Pavement Inlays." Ph.D. Dissertation, University of Illinois Urbana-Champaign, Urbana, IL.
- Bordelon, A., and Roesler, J. "Flowable Fibrous Concrete for Thin Concrete Inlays." *Proc., Transportation and Development Institute Congress*, 874-883.
- Bordelon, A. C., and Roesler, J. R. (2014). "Spatial Distribution of Synthetic Fibers in Concrete with X-Ray Computed Tomography." *Cement and Concrete Composites*, 53, 34-43.
- Cervantes, V., and Roesler, J. (2009). "Performance of concrete pavements with optimized slab geometry." *Urbana*, 51, 61801.
- Chanvillard, G., Aitcin, P., and Lupien, C. (1989). "Field evaluation of steel fiber reinforced concrete overlay with various bonding mechanisms." *Transportation Research Record: Journal of the Transportation Research Board*(1226), 48-56.
- Darter, M. I., and Barenberg (1977). "Design of a Zero-maintenance Plain Jointed Concrete Pavement, Volume One-Development of Design Procedures."
- de Oliveira e Sousa, J. L. A., and Gettu, R. (2006). "Determining the tensile stress-crack opening curve of concrete by inverse analysis." *Journal of engineering mechanics*, 132(2), 141-148.
- Delatte, N. J., Williamson, M. S., and Fowler, D. W. (2000). "Bond strength development with maturity of high-early-strength bonded concrete overlays." *ACI Materials Journal*, 97(2), 272-280.
- Emmons, P. H., Czarnecki, L., McDonald, J. E., and Vaysburd, A. "Durability of repair materials: Current practice and challenges." *Proc., International symposium on brittle matrix composites*, 263-274.

- Gaedicke, C., and Roesler, J. (2009). "Fracture-based method to determine the flexural load capacity of concrete slabs." *FAA COE Rep*(31).
- Gilbert, R., Bradford, M., Gholamhoseini, A., and Chang, Z.-T. (2012). "Effects of shrinkage on the long-term stresses and deformations of composite concrete slabs." *Engineering Structures*, 40, 9-19.
- Granju, J. (1996). "Thin bonded overlays: about the role of fiber reinforcement on the limitation of their debonding." *Advanced Cement Based Materials*, 4(1), 21-27.
- Grzybowski, M., and Shah, S. P. (1990). "Shrinkage cracking of fiber reinforced concrete." *ACI Materials Journal*, 87(2), 138-148.
- Guo, X., Tin-Loi, F., and Li, H. (1999). "Determination of quasibrittle fracture law for cohesive crack models." *Cement and concrete research*, 29(7), 1055-1059.
- Harrington, D. (2008). "Guide to concrete overlays." *National Concrete Pavement Technology Center. Ames, IA*.
- Hillerborg, A. (1985). "The theoretical basis of a method to determine the fracture energy G_F of concrete." *Materials and structures*, 18(4), 291-296.
- Jenq, Y., and Shah, S. (1986). "Crack propagation in fiber-reinforced concrete." *Journal of Structural Engineering*, 112(1), 19-34.
- Khazanovich, L., Buch, N., and Gotlif, A. (2001). "Evaluation of alignment tolerances for dowel bars and their effects on joint performance." Michigan State University, Pavement Research Center of Excellence.
- Khazanovich, L., Hoegh, K., and Snyder, M. B. (2009). *Guidelines for dowel alignment in concrete pavements*, Transportation Research Board.
- Kim, M. O., and Bordelon, A. (2015). "Determination of Total Fracture Energy for Fiber-Reinforced Concrete." *ACI Special Publication*.
- Kim, M. O. (2016). "Effect of Fiber-Reinforced Concrete in Thin Overlays." Ph.D. Dissertation, University of Utah, Salt Lake City, UT.
- Kim, M. O., and Bordelon, A. (2016). "Fiber effect on interfacial bond between concrete and fiber-reinforced mortar." *Transportation Research Record: Journal of the Transportation Research Board*(2591), 11-18.
- Kim, M. O., and Bordelon, A. (2017). "Age-dependent properties of fiber-reinforced concrete for thin concrete overlays." *Construction and Building Materials*, 137, 288-299.
- Lange, D., and Shin, H.-C. (2001). "Early age stresses and debonding in bonded concrete overlays." *Transportation Research Record: Journal of the Transportation Research Board*(1778), 174-181.
- Levy, C. (2010). "Numerical Investigation of the Effects of Shrinkage and Thermal Loading on the Behaviour of Misaligned Dowels in Jointed Concrete Pavement."
- Li, V. C., Stang, H., and Krenchel, H. (1993). "Micromechanics of crack bridging in fibre-reinforced concrete." *Materials and structures*, 26(8), 486-494.

- Mangat, P., and Azari, M. M. (1988). "Shrinkage of steel fibre reinforced cement composites." *Materials and Structures*, 21(3), 163-171.
- McCullough, B., and Dossey, T. (1999). "Considerations for high-performance concrete paving: Recommendations from 20 years of field experience in Texas." *Transportation Research Record: Journal of the Transportation Research Board*(1684), 17-24.
- Mehta, P. K., and Monteiro, P. J. (2006). *Concrete: microstructure, properties, and materials*, McGraw-Hill New York.
- Mindess, S., Young, J. F., and Darwin, D. (2002). *Concrete*, Prentice Hall.
- Momayez, A., Ramezani-pour, A., Rajaie, H., and Ehsani, M. (2004). "Bi-surface shear test for evaluating bond between existing and new concrete." *ACI Materials Journal*, 101(2), 99-106.
- Park, K., Paulino, G., and Roesler, J. (2008). "Determination of the kink point in the bilinear softening model for concrete." *Engineering Fracture Mechanics*, 75(13), 3806-3818.
- Rasmussen, R. O., and Rozycki, D. K. (2004). *Thin and ultra-thin whitetopping: A synthesis of highway practice*, Transportation Research Board.
- Roesler, J., Paulino, G., Gaedicke, C., Bordelon, A., and Park, K. (2007). "Fracture behavior of functionally graded concrete materials for rigid pavements." 40-49.
- Roesler, J., and Wang, D. (2008). "An analytical approach to computing joint opening in concrete pavements." *Pavement Cracking: Mechanisms, Modeling, Detection, Testing and Case Histories*, 79.
- Roesler, J. R., Bordelon, A., Ioannides, A., Beyer, M., and Wang, D. (2008). "Design and concrete material requirements for ultra-thin whitetopping." Illinois Center for Transportation.
- Sanjuan, M. (1999). "Effect of low modulus sisal and polypropylene fibre on the free and restrained shrinkage of mortars at early age-Optimisation to control plastic shrinkage." *Cement and Concrete Research*, 29(10), 1597-1604.
- Sevil, T., Baran, M., Bilir, T., and Canbay, E. (2011). "Use of steel fiber reinforced mortar for seismic strengthening." *Construction and Building Materials*, 25(2), 892-899.
- Snyder, M. B. (2011). "Guide to dowel load transfer systems for jointed concrete roadway pavements."
- Song, P., Hwang, S., and Sheu, B. (2005). "Strength properties of nylon-and polypropylene-fiber-reinforced concretes." *Cement and Concrete Research*, 35(8), 1546-1550.
- Sprinkel, M. M., and Ozyildirim, C. (2000). "Evaluation of hydraulic cement concrete overlays placed on three pavements in Virginia."
- Swamy, R., and Stavrides, H. "Influence of fiber reinforcement on restrained shrinkage and cracking." *Proc., ACI Journal proceedings*, ACI, 443-460.
- Tayeh, B. A., Bakar, B. A., Johari, M. M., and Voo, Y. L. (2012). "Mechanical and permeability properties of the interface between normal concrete substrate and ultra high performance fiber concrete overlay." *Construction and Building Materials*, 36, 538-548.

- Tschegg, E. (1991). "New equipments for fracture tests on concrete." *Journal of Material Testing*, 33, 338-342.
- Vaysburd, A., and Emmons, P. (2000). "How to make today's repairs durable for tomorrow—corrosion protection in concrete repair." *Construction and building materials*, 14(4), 189-197.
- Wang, Y., Li, V. C., and Backer, S. (1990). "Experimental determination of tensile behavior of fiber reinforced concrete." *ACI Materials Journal*, 87(5), 461-468.
- Zollo, R. F. (1997). "Fiber-reinforced concrete: an overview after 30 years of development." *Cement and Concrete Composites*, 19(2), 107-122.